DESIGN OF MATERIALS FOR BIOSENSORS AND ENERGY STORAGE

By

JARRYD NOAH ASHBY

(Under the Direction of Ramaraja Ramasamy)

ABSTRACT

Due to diminishing available petroleum resources, alternative sources of power storage have become ever more necessary. Since the discovery of lithium-ion batteries in the 1970s and the first commercialized material (lithium cobalt oxide), research in this field has exploded. Herein is described the synthesis methods and morphologies of several lithium iron phosphate morphologies, one of which is lithium iron phosphate nanobelts, along with the synthesis of pyridine functionalize graphene. The crux of which involves maximization of the primary channel of lithium-ion diffusion within the material via excess chloride, an ion which lends to inhibiting particle growth of the material in the <010> direction, within the precursor solution, as well as maximizing the aspect ratio of the material, and subsequently modifying the material with nitrogen-doped graphene materials to act as a conducting agent. Additionally is explored the effectiveness of a copper titanate anode. Finally, a cholesterol oxidase biosensor is discussed.

DESIGN OF MATERIALS FOR BIOSENSORS AND ENERGY STORAGE

by

JARRYD NOAH ASHBY

BS, Clemson University, 2010

A Thesis Submitted to the Graduate Faculty of The University of Georgia in Partial Fulfillment of the Requirements for the Degree

MASTER OF SCIENCE

ATHENS, GEORGIA

2017

DESIGN OF MATERIALS FOR BIOSENSORS AND ENERGY STORAGE

by

JARRYD NOAH ASHBY

Major Professor:	Ramaraja Ramasamy
Committee:	John Stickney
	Jeffrey Urbauer

Electronic Version Approved:

Suzanne Barbour
Dean of the Graduate School
The University of Georgia
August 2016

TABLE OF CONTENTS

LIST OF FIGURES

CHAPTER 1

LITHIUM-ION BATTERIES

Introduction

Because of the dwindling petroleum resources and their vilification as a result of global warming, and additionally as a result of the limitations of renewable energy sources, methods of energy storage have become all the more desired for the consumer market and public sector. Lithium batteries were first made available for use in the 1970s when Adam Heller patented a cathode of a lithium battery consisting of a liquid thionyl chloride cathode and a lithium metal anode. [1] This material still exists in military applications for portable electronics and memory backup due to its tremendous energy density and efficacy at low temperatures; however, this material is exceptionally toxic and the risk of explosion when shorted is tremendous. In 1976, M.S. Whittingham proposed a titanium sulfide cathode material with a lithium anode while working at Exxon.[2] This material had the drawback of being fabulously expensive. In 1980, John Goodenough and Koichi Mizushima demonstrated the use of lithium cobalt oxide as the use of the first economically practical lithium-ion cathode material.[3]

Lithium-ion batteries utilize lithium ions in the electrolyte as their source of lithium, rather than lithium batteries due to the limitation of lithium metal where dendrites form until they reach the opposite electrode, shorting the battery. The battery then undergoes thermal runaway and creates

the risk of explosion.[4] Figure 1.1 shows a generic schematic of charge and discharge in a lithium ion battery.[5]

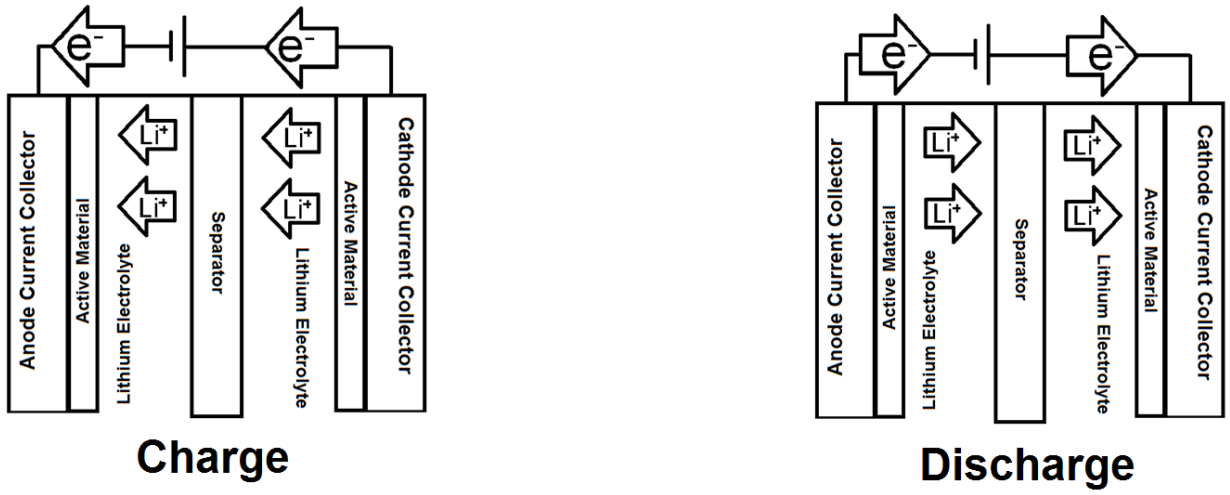

Figure 1.1 Schematic of charge and discharge of lithium-ion cell

The effectiveness of a lithium ion battery requires three paramount qualities: good specific capacity, high coulombic efficiency, and good rate capability. Specific capacity is defined by the amount of amp-hours that can be drawn from a material across its operating voltage range per gram of material.[6] Coulombic efficiency with respect to batteries is the energy that can be drawn from it versus the amount of energy that can be put in to it. This ties most closely to the lifetime and cyclability of a battery, where a coulombic efficiency of 1 would mean that the battery would never die, and a coulombic efficiency of 0.999 would mean that the battery loses 0.1% of its capacity every cycle.[6] The rate capability of a battery pertains to the maximum rate at which power can be drawn from the battery safely and without tremendous loss of capacity. A high rate means high power, and to the application of the electric automotive industry and other high

power applications, the ability to draw a large amount of energy immediately becomes imperative.[7] In this case then, further improvement of existing materials, as well as the development of new materials is essential, while improving or maintaining safety as well.

Methods for Improving Electrode Materials

One such method of improving battery materials is through the use of electrolyte additives that allow the battery to operate at the higher voltages normally associated with oxidation of the electrolyte that causes electrode degradation and thermal runaway.[8-11] An issue this can also help prevent, which often occurs in batteries, especially with batteries connected in series where capacity between each cell is difficult to homogenize, is overcharging.[8] The additives oxidize and reduce at the electrode surfaces reversibly in order to prevent the electrolyte itself from reaching the electrode and doing so itself.[12]

Another method to improve the rate capability of lithium-ion batteries is through the use of supervalent doping of the materials. This has the possibility of improving the efficacy of batteries by two venues. The first is by expanding channels for lithium ion diffusion such that lithium ions can move through the material more easily. The second is through electronic induction that improves charge transfer through the material.[13-15] This does, however, present loss of capacity when other metals are doped in favor of lithium, as well as for the case of one-dimensional diffusion materials, create the possibility of shrinking diffusion pathways and lowering ionic conductivity.[16] Additionally, anion doping has also been shown to improve the electrochemical performance of materials at the risk of structural changes.[17-19]

Metal coatings can also be used to improve cycling characteristics of electrode materials. Metals which are chemically inert within the voltage window of the electrodes operation (for example copper and silver on cathodes), add a conductive conduit for electrons on the material. The problem with this, however, is that metal coatings are difficult to homogenize and the metals themselves are expensive, especially relative to cheap electrode materials like lithium iron phosphate.[18, 20]

Carbon coating, in effect, provides a conduit for electrons to flow quickly from the active material to the current collector. Conversely, in the absence of a carbon coating, the electrons from the oxidation and reduction of the metal centers of the material are relegated to flowing solely through the material itself. This is a particular problem in common cathode materials where the majority are nearly insulating semiconductors. Figure 1.2 shows a schematic of the general electron flow through the active material and carbon coating and how the coating aids conductivity of the bulk material.[21] This also has the effect of improving the voltage profile of a material by lowering the rate at which the internal resistance increases in the material relative to the depth of lithiation or delithiation.[18]

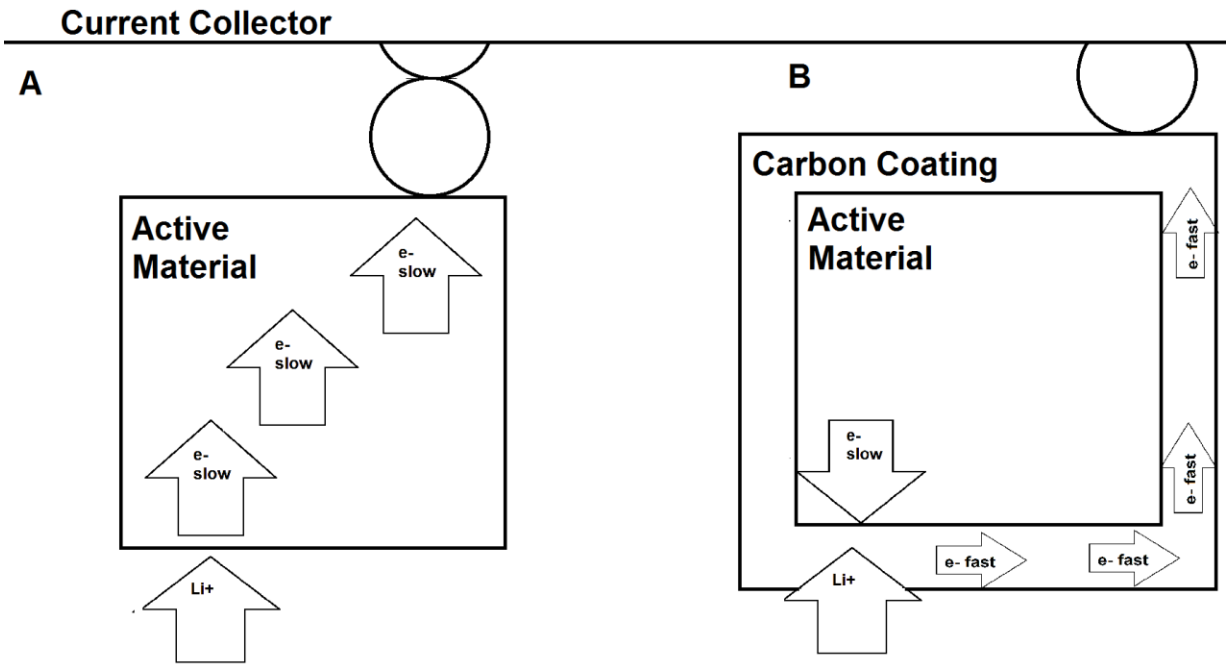

Figure 1.2 Schematic of effect on electron flow in the absence, *A*, and presence, *B*, of carbon coating

The tradeoff to this method is the loss of specific capacity of the material, to wit, the decrease in active material relative to the total mass of the film. As it is that carbon has no cathodic activity, with the exception of lithium carbide in specific circumstances, the capacity of the cell decreases with respect to the mass content of carbon.[22] Further, while this addresses the low electronic conductivity, the addition of carbon says nothing to the ionic conductivity of the material.[23] Additional challenges with carbon coating include the homogeneity of the coating, the ratio of sp^2/sp^3 carbon in the coating, the H/C ratio in the carbon coating, where lower is better in both of the former cases, and the thickness of the coating.[24-25]

A facile method of improving performance is metal fluoride coatings, such as aluminum fluoride. This method operates on a similar principle to carbon coating whereby aluminum fluoride is adhered and subsequently annealed with the cathode material. Such a coating

decreases charge transfer resistance like carbon coating and maintaining that over several cycles, i.e. prohibiting corrosion of the cathode material due to the electrolyte, as well as decreasing the amount of metal lost from the cathode material to the electrolyte (an unwanted side product). Additionally, in the case of high voltage cathodes, this carries the benefit of mitigating the formation of a surface-electrolyte interface on the cathode surface that occurs at higher voltages.[26-27]

CHAPTER 2

LITHIUM IRON PHOSPHATE

STUDIES IN MORPHOLOGY AND ENHANCING MATERIALS

Introduction

Relative to more energy dense cathode materials, lithium iron phosphate possesses a few distinct advantages, the paramount of which is the inherent safety of the material.[6, 28-31] Further, they are innocuous to the environment, possess a high, flat voltage plateau for lithium inseration and removal, and the precursors are inexpensive relative to alternatives cathode materials such as $LiCoO_2$.[28-32] Figure 2.1 shows a comparison of lithium iron phosphate to several cathode materials.

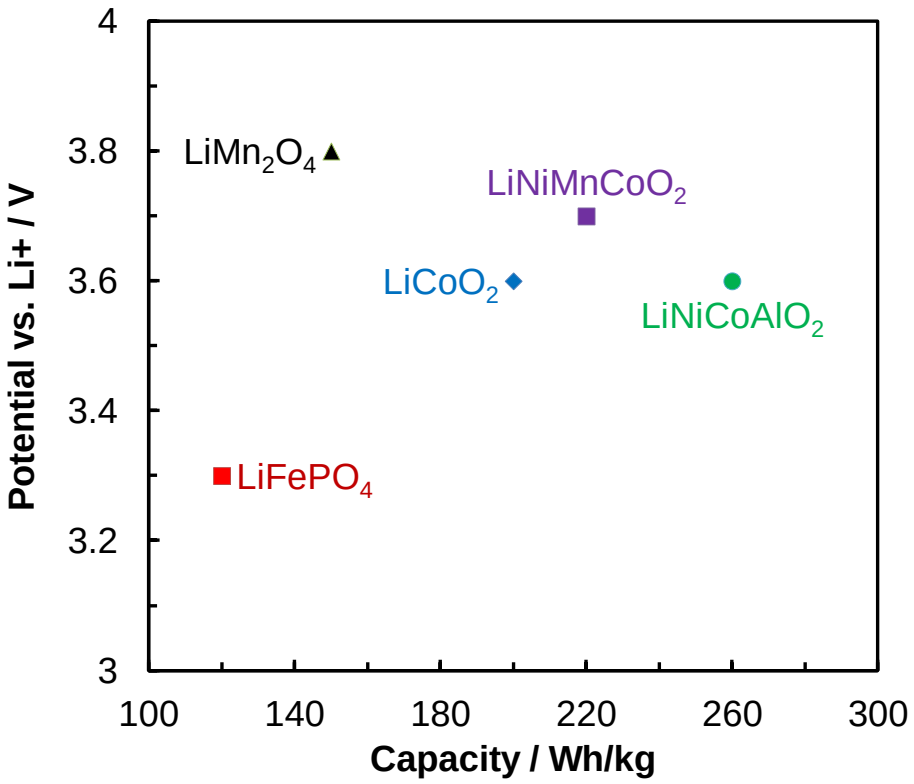

Figure 2.1 Comparison of several cathode materials by nominal voltage and capacity. [33,34]

The inherent safety of the material stems from the operating voltage sitting well below the upper voltage threshold for the surface-electrode interface layer formation as a result of degradation of the electrolyte.[26] A schematic of the HOMO-LUMO gap whereby SEI layers are formed and the operating voltage of several electrodes is shown in Figure 2.2**.**

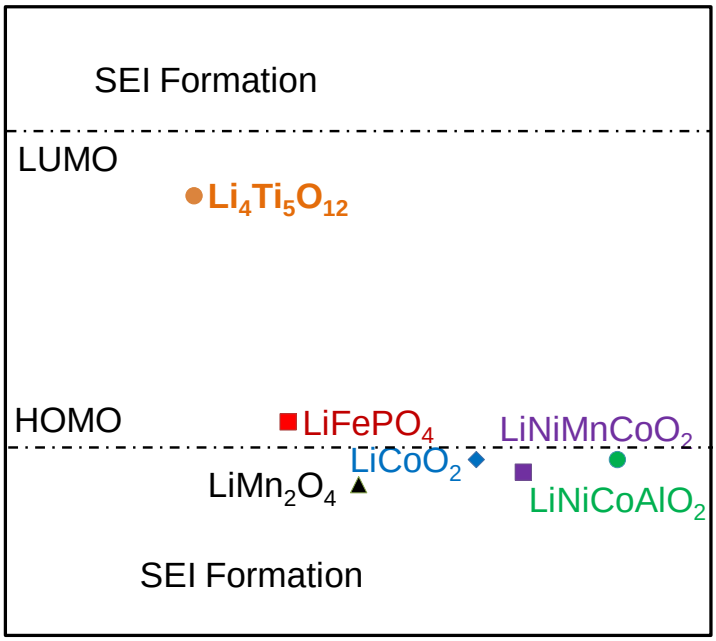

Figure 2.2 Diagram of the HOMO-LUMO gap of typical electrolytes and how several electrodes compare[33]

A difficulty that occurs in the utilization of lithium iron phosphate as a cathode material is its inherently poor conductivity. This is the case in all polyanionic cathode materials generally; however, in the case lithium iron phosphate this is especially true, and along with its average specific capacity, is its primary limitation. Another cumbersome limitation to lithium iron phosphate is that it possesses a one-dimensional channel for lithium ion diffusion: <010>.[35-38] This is particularly true on the micro/nano-scopic scale, where diffusion on the b-axis wherein the migration energy along said axis is 0.57 eV, compared to 2.89 eV and 3.36 eV for <001> and <101>, respectively.[35] On the large-scale, however, the rate of chemical diffusion becomes nearly the same in all directions. Additionally, the rate of diffusion decreases by one-hundred fold, even at elevated temperatures.[39] Figure 2.3 illustrates mechanism for superior lithium diffusion in small particles. It is shown that by reducing the particle size, size effects play a part

such that the energy required to generate a single phase diffusion through the material is possible. By doing so, the <010> channels are fully occupied rather than the ones at the $LiFePO_4/FePO_4$ interface in the two-phase growth system.[40]

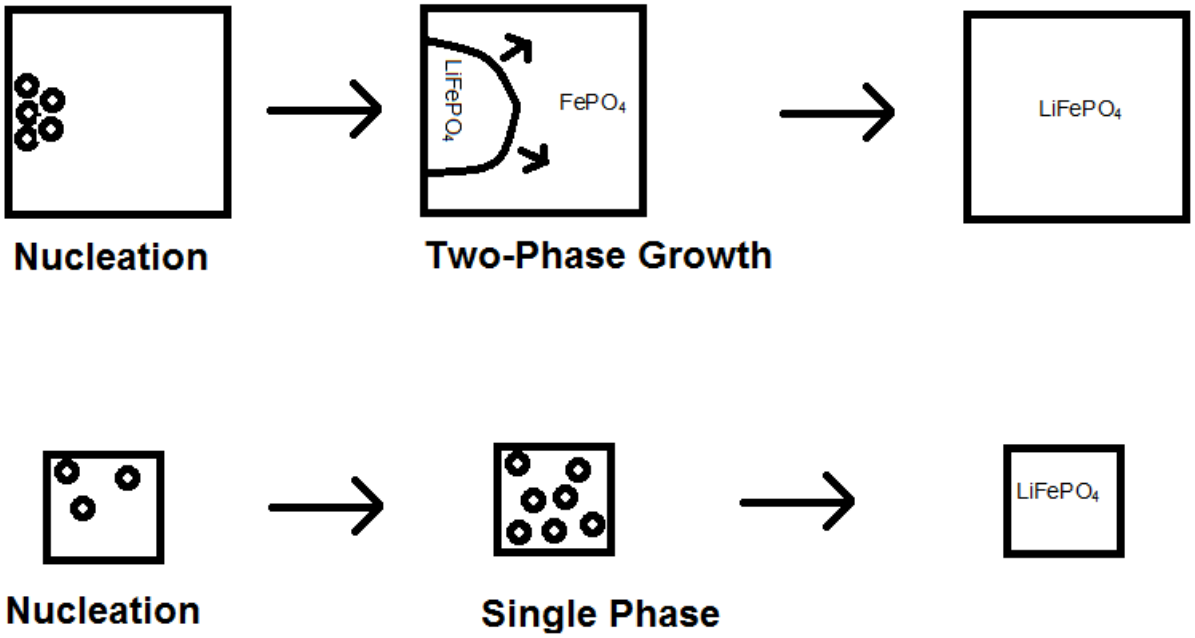

Figure 2.3 Schematic of isotropic and anisotropic lithium insertion in Lithium Iron Phosphate[40]

Another issue with one-dimensional diffusion materials such as lithium iron phosphate is the problem of point defects, whereby the diffusion channel in the lattice is occupied by a foreign metal ion (in this case iron). To remedy this, annealing to improve crystallinity, and particle size reduction are common.[32, 41-42] The reduction of particle size follows that by shortening the length of the respective channels for lithium ion diffusion, the incidence of iron point defects in lithium positions in the lattice become less relevant regardless of their occurrence. For example, if a channel would ordinarily be occupied by four lithium ions by intercalation, and this extends to all particles within the bulk, and an iron occupies the third position within the channel from the

outside, the loss of positions would be half; however, in the case that the channel would be occupied by four hundred ions and an iron occupies even the two hundred position, while the percentage of positions lost would be the same, the discharge voltage, and subsequently, power, lost to this effect would be far more substantial, as the time required to occupy two spaces per particle throughout the bulk material.[43] In fact, the particle size has a far greater correlation to the specific capacity and charge transfer resistance than does the presence of an aid, such as carbon coating, when the scale is particularly small.[40, 44] The drawback of this method, however, is a decrease in the tap density, defined as the volume occupied by a given mass upon tapping down the material within a vessel, of the bulk material.[45] Figure 2.4 presents a cross-section of the lithium iron phosphate diffusion channels demonstrating the single channel of diffusion, as well as the effect of point defects in the lattice.[43]

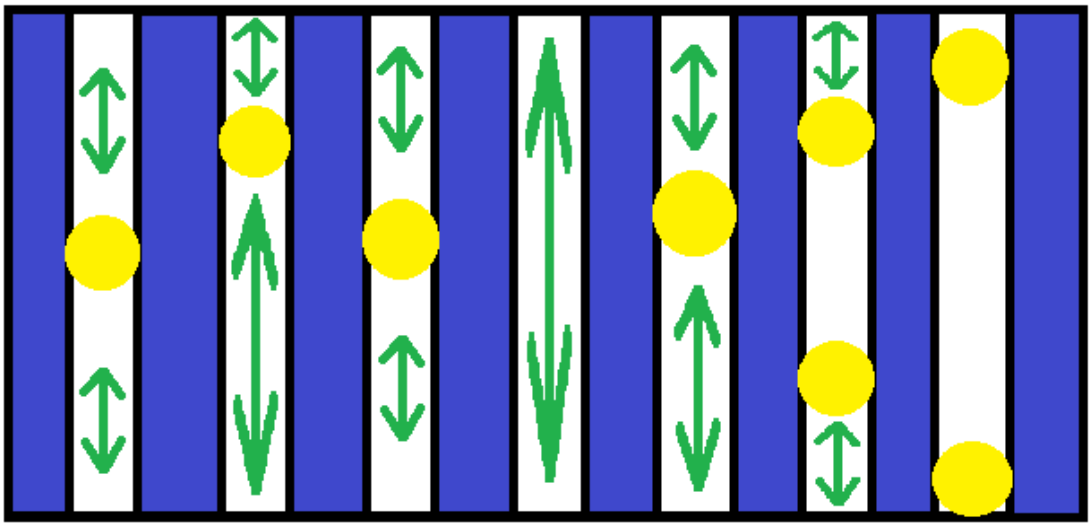

Figure 2.4 Cross-section of Lithium Iron Phosphate crystal structure showing the one-dimensional channel for lithium ion diffusion, and the effect of point defects (*yellow*), on diffusion (*green*).[43]

In the following sections morphological studies based on changes of the precursor cocktail as well as changes in the solvent used in the reaction are explored. Additionally a novel carbon additive for improved packing and cycling characteristics is described.

Experimental

Lithium iron phosphate materials were produced via a solvothermal synthesis method in diethylene glycol.[46] The reagents therein were stoichiometrically normalized in proportion to the molar content of Fe (II) ions added, in most cases, from iron (II) chloride. Chloride ion content was controlled via potassium chloride, lithium chloride, and the previously mentioned iron (II) chloride, and lithium, which is always presented in excess to help mitigate the instance of iron point defects in the crystal lattice of the product, lithium iron phosphate, are provided by lithium dihydrogen phosphate, and lithium chloride. Additionally, the presence of chloride has been reported to discourage growth in the <010> facet.[46] Hydroxide was introduced to the precursor as potassium hydroxide in stoichiometric amounts, likewise relative to iron. To prevent the oxidation of iron in the precursor solution, argon was purged through the solvent during preparation of the precursor, further supplemented by the addition of ascorbic acid at 5% by mass versus iron chloride. After dissolution of all reagents, the precursor solution was added to a Teflon lined steel autoclave and heated in an oven at 210 °C for 24 hrs. The resulting solution was then washed via centrifugation in ethanol and water multiple times to remove residual salts. As schematic of protocol is given in Figure 2.5.

Reagents → / Protocol ↓	LiCl	$FeCl_2$	LiH_2PO_4	$FeSO_4$	KCl
L2Cl3	1	1	1	0	0
L2Cl4	1	1	1	0	1
L2Cl5	1	1	1	0	2
L2Cl6	1	1	1	0	3
L3Cl3	2	0.5	1	0.5	0
L3Cl4	2	1	1	0	0
L3Cl5	2	1	1	0	1
L3Cl6	2	1	1	0	2

Figure 2.5 Reaction Schematic for lithium iron phosphate synthesis wherein the stoichiometry of the precursors was normalized to the molar amount of iron. The precursor is likewise modified under that same restriction with potassium hydroxide to study the effect of said reagent on the formation of structures.

In addition to this, studies of the morphological formations of the powders from this reaction were studied with respect to the solvent used. After optimizing the reaction with respect to diethylene glycol, ethylene glycol, water, Triton X-100, and glycerol were examined in the same optimized proportions. Confirmation of the presence of lithium iron phosphate was done by X-ray diffraction, and the morphology was analyzed by scanning electron microscopy.

In addition, a carbon coating was applied to one sample of the material by suspending the LFP powder in a solution of sucrose in ethanol and water and sonicating. Followed by drying and subsequently annealing at 550 °C for four hours. The result of this was analyzed by SEM and is shown and discussed in the following section and Figure 2.14.

After obtaining lithium iron phosphate structures that resemble nanosheets, or in this case, nanobelts, the material was modified with pyridine-functionalized graphene (PyG) for the purpose of firstly, enhance ordering of the material with respect to the total structure of the

powder as a cathode, which would, thus, enhance specific capacity with respect to the active material. Secondly, in lieu of the introduction of a conductive material, graphene, to the cathode it would enhance the conductivity of the superstructure without the need for the labor associated with carbon coating. A schematic of this is given in Figure 2.6.

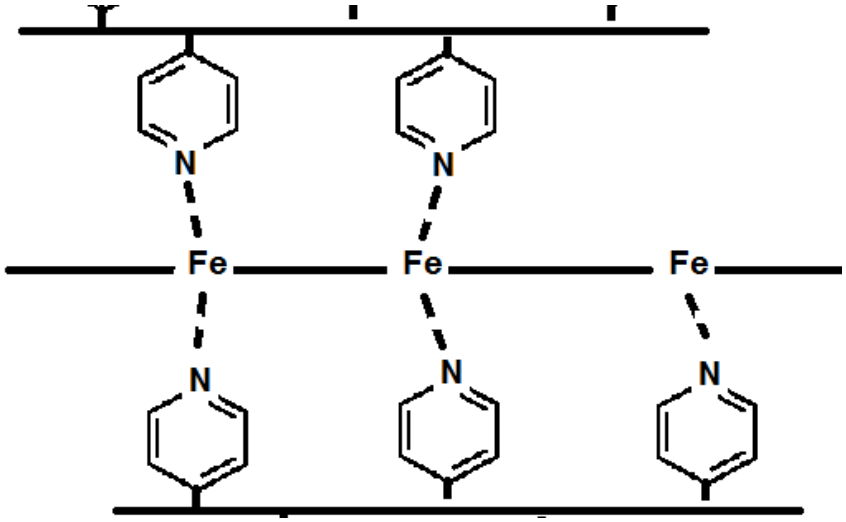

Figure 2.6 Schematic of pyridine-functionalized graphene (PyG) grafted with lithium iron phosphate nanosheets

Pyridine-functionalized graphene (PyG) was synthesized by a pyridinium salt reaction whereby sodium nitrite and 4-aminopyridine were combined in deionized water at 0°C. First, sodium nitrite was dissolved in deionized water. Second, 4-aminopyridine was added to a separate amount of deionized water, at which point concentrated hydrochloric acid was added to the solution until the solid dissolved. After this, the sodium nitrite solution was added drop-wise to the 4-aminopyridine and left to stir for thirty minutes. In many cases, this results in the precipitation of a solid. This is unfavorable, thus, additional hydrochloric acid was added such that a yellow colored solution resulted. This precursor was added drop-wise to a suspension of reduced graphene oxide in dimethyl formamide at 0°C, where it was then kept at 0°C under

stirring for four hours and then allowed to reach room temperature and react for an additional sixteen hours.[47,48] The resulting solution was filtered vacuum filtration and subsequently taken up in 1 M sodium hydroxide for an additional day to quench the reaction and filtered again. The product was analyzed by FT-IR.

The lithium iron phosphate cathodes were tested via coin cell fabrication using CR 2032 coin cells from MTI Corporation. The electrolyte used was lithium hexaflurophosphate in a 1:1, by volume, solution of ethylene carbonate and diethylene carbonate. A schematic of the coin cell fabrication set up is shown in Figure 2.7.

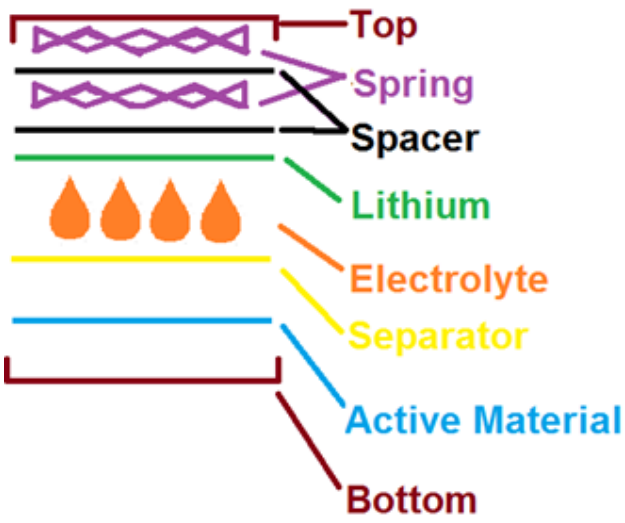

Figure 2.7 Schematic of Coin Cell Assembly. Coin cells were fabricated by centering the active material, then layering and centering the separator material, followed by several drops of electrolyte solution, and subsequently layering and centering the lithium anode, spacer, spring, spacer, spring, and top, respectively.

Before fabrication of the cells, however, the lithium iron phosphate powders were dried under vacuum for two hours at 120 °C. The powder was then combined in an 8:1 proportion by mass with Super-P carbon and ground together in an agate mortar. Afterwards, this powder was added

to a solution of polyvinylidene difluoride (PVDF) in n-methyl pyrrolidone (NMP), whereby the concentration of PVDF constitutes an amount such that the final proportion by mass of the materials used are 8:1:1 active:carbon:PVDF. Additional NMP was subsequently added to the slurry to reduce the viscosity therein to the point of a flowing appearance of warm syrup. After homogenizing the slurry via stirring for a minimum of thirty minutes, it was then incrementally spread on an aluminum current collector foil, and then further spread to a uniform film by a doctor blade. Finally, the foil was dried under vacuum at 80 °C overnight, then pressed at 3000 psi.[33, 49]

Material Fabrication Results and Discussion

Chloride Dependent Studies

The scanning electron micrographs from Figure 2.8 demonstrate that beyond a certain threshold of chloride ions in the precursor solution (≥4) the morphology of the material becomes immaterial to the content of chloride salt therein.

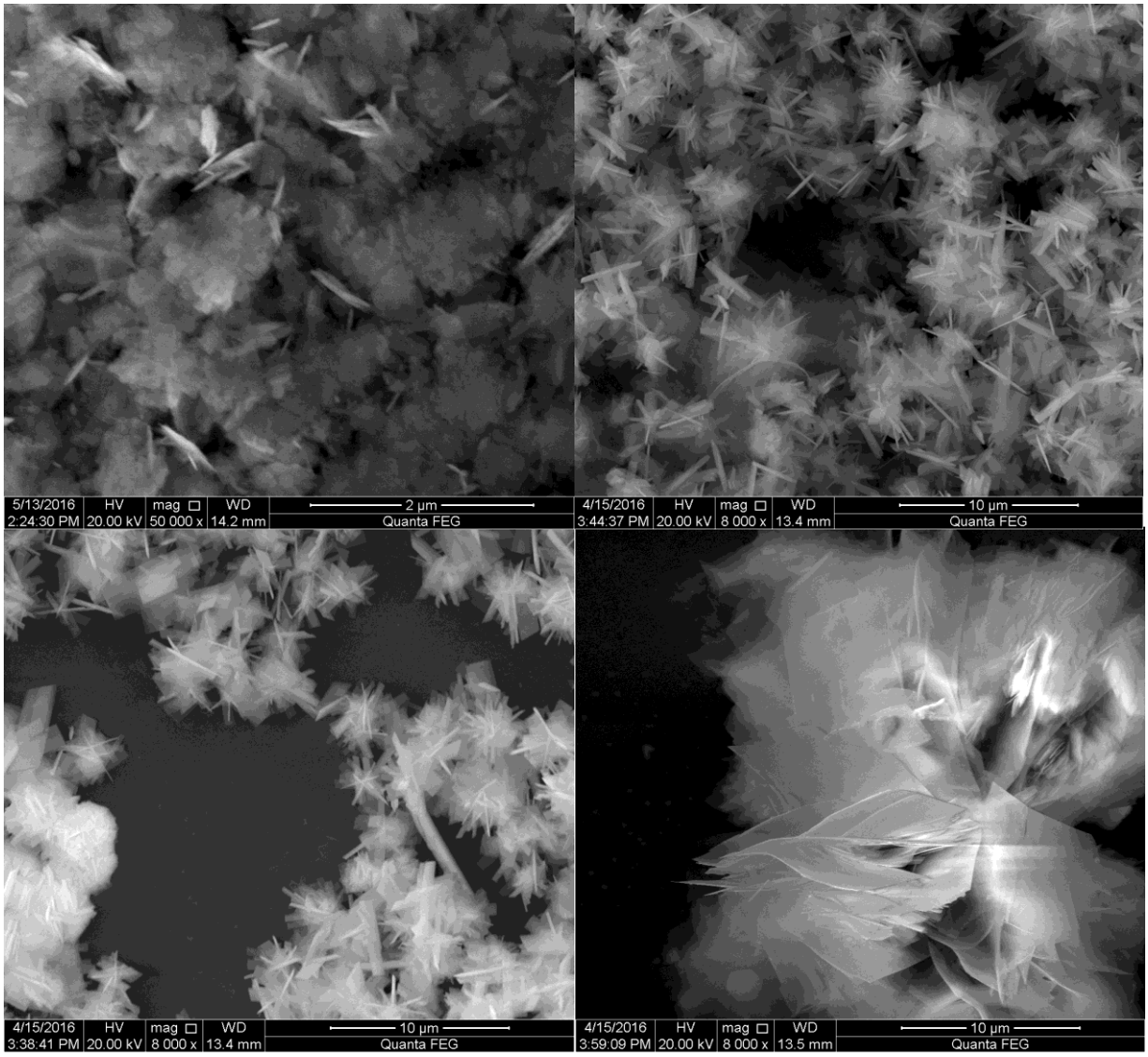

Figure 2.8 Scanning Electron Micrographs for lithium iron phosphate syntheses using varying chloride concentrations *Left to Right (Top):* Cl:Fe 3:1, 4:1, *Left to Right (Bottom):* 5:1, and 6:1

Beyond five equivalents of chloride salt, the powders abandon the belt morphology and adopt a non-homogeneous array of large sheet aggregates, small plates, and peapod shapes as shown in Figure 2.9.

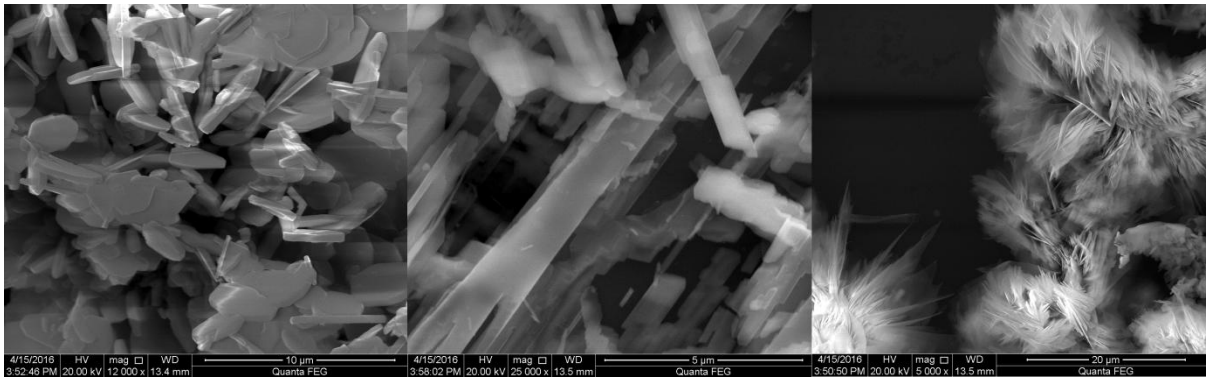

Figure 2.9 Scanning electron micrographs of one sample of lithium iron phosphate from the protocol utilizing 6:1 Cl:Fe demonstrating a non-homogeneous morphology.

Hydroxide Dependent Studies

The precursor was modified by increasing additions of potassium hydroxide before addition of solvent and iron (II) chloride. The addition of the iron precursor precipitated a dark green suspension with increasing hydroxide content indicating the formation of iron (II) hydroxide in amounts concurrent with the amount of potassium hydroxide added. The addition of lithium diphosphate turned the suspension immediately white. Shown in Figure 2.10 is the scanning electron micrographs of the powders formed from these syntheses.

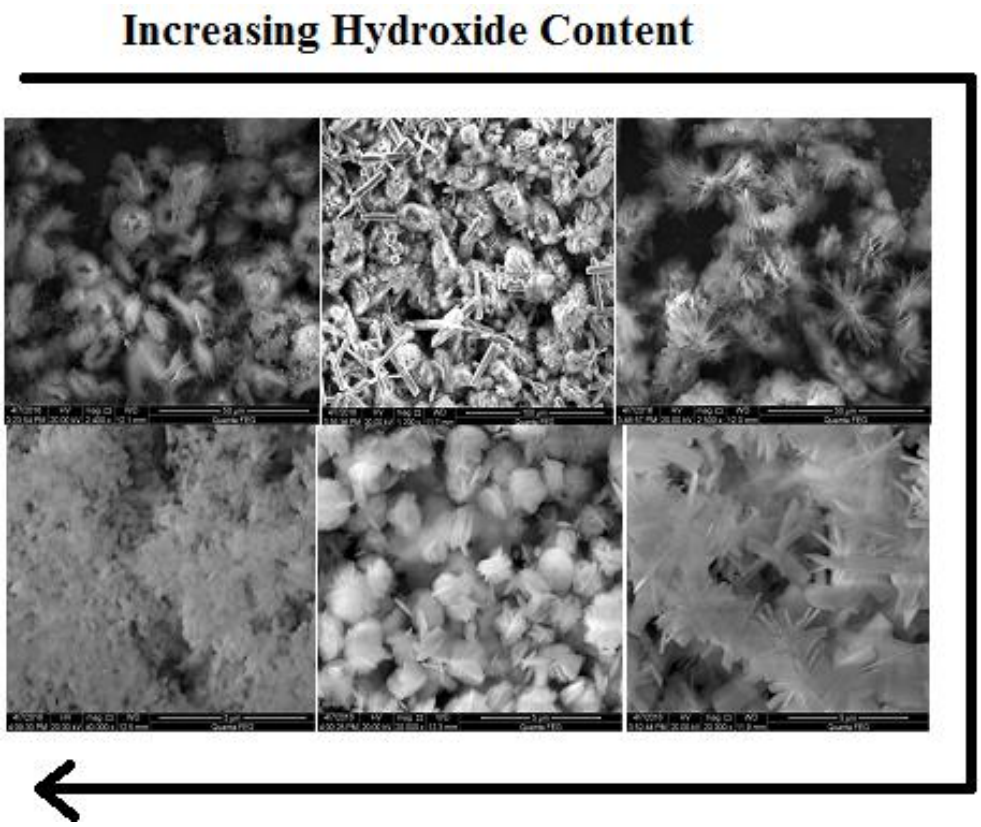

Figure 2.10 Scanning Electron Micrographs of lithium iron phosphate with varying hydroxide content in the precursor solution *From top left:* (OH:Fe) 0:1, 0.25:1, 0.5:1, 0.75:1, 1:1, and 2:1, respectively.

With no addition of hydroxide to the precursor, the powders form bird nest like structures; however, upon the addition of 0.25 stoichiometric equivalents relative to iron, the resultant powders contain rods as well as those same bird nests. Half an equivalent results in dumbbell-like structures in homogeneous yield.[50] Between 0.6 and 0.8 equivalents forms nanobelts of likewise homogeneous yield. Beyond that, the penultimate powder examined are agglomerates of plates, or possibly sheets, and the ultimate, oblong beads.

In an effort to examine the nanobelts individually, and to make them conducive to later modification, sonication was attempted on the powders (from L2Cl5 protocol with 0.7

equivalents of hydroxide). The result of this is shown in Figure 2.9. Unfortunately, the end result of sonication of these powders simply resulted in the destruction of the belts rather than anything resembling exfoliation for the most part.

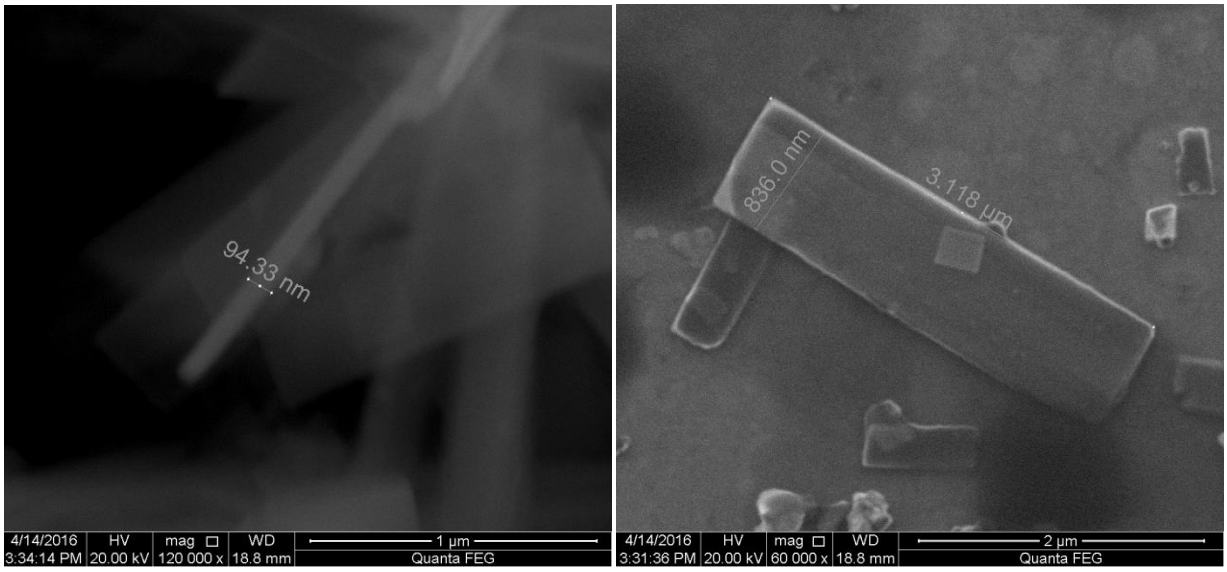

Figure 2.11 Magnified view of the lithium iron phosphate nanobelt SEM. The thickness of the belts ranges from 60 to 100 nm in all tested samples

Fortuitously, however, it was found that the act of exfoliating the material was largely unnecessary, as the simple mechanical disturbance of slurry fabrication managed to exfoliate the belts into singular units, as per the micrographs in Figure 2.17.

Repeatability

The protocol for the synthesis of the nanobelts was repeated several times and an example of the efficacy of the protocol is shown in Figure 2.12. In each case, the <020> peak at ~30° exists at a greater intensity than the <200> peak at ~17°, which indicates an, at least, plate-like structure.[51] Further, the high signal-to-noise ratio indicates an adequate degree of crystallinity in the material.

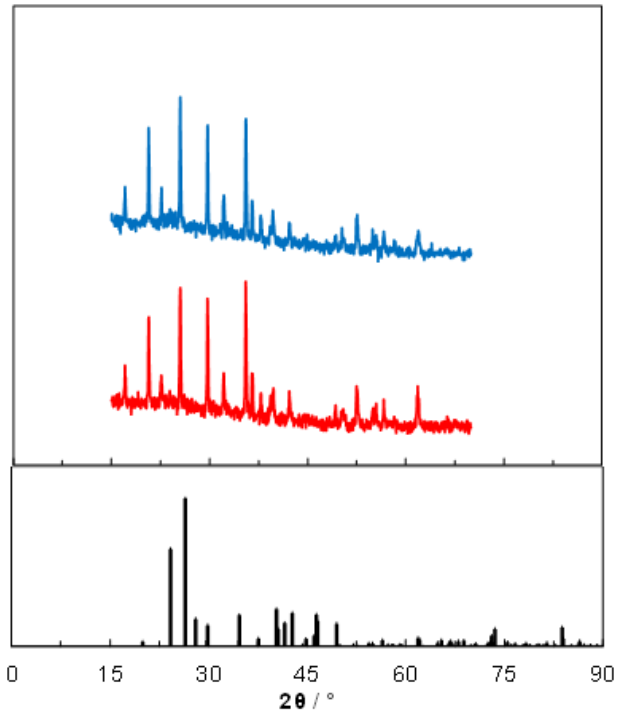

Figure 2.12 X-Ray Diffraction Patterns of two separate preparations of the lithium iron phosphate nanobelts under the same synthesis conditions, indicating a high degree of repeatability (The protocol was repeated in excess of five times).

Solvent Dependent Studies

The effect of the solvent used on the morphology of the powders in the optimized diethylene solvothermal synthesis was also examined. Ethylene glycol, a commonly used solvent for solvothermal synthesis, particularly for earlier syntheses of lithium iron phosphate, was employed and the results showed that similarly to the 1:1 potassium protocol discussed previously, the material produced was thin agglomerates of sheets; however, they exist in more randomized shape than in the case of diethylene glycol. Triton X-100 was also employed and exhibited an extremely randomized morphology from the dumbbell-like structures shown in Figure 2.8, to long thick wires. Glycerol, most interestingly, produced the same morphology as diethylene glycol; however, the belts examined appeared to be a relatively smaller than the ones produced from DEG. When water was employed as the solvent, regardless of hydroxide content, the produced morphology was either rectangular prismatic, or large irregular masses. This could potentially be attributed to the shift in pH of the solution as more of the material crystallizes and precipitates from the solution, whereby the only sustenance for the pH, which in water is the only impetus for the suspension of the material for growth, is the phosphate ion. The scanning electron micrographs for the materials produced from these protocols are given in Figure 2.13.

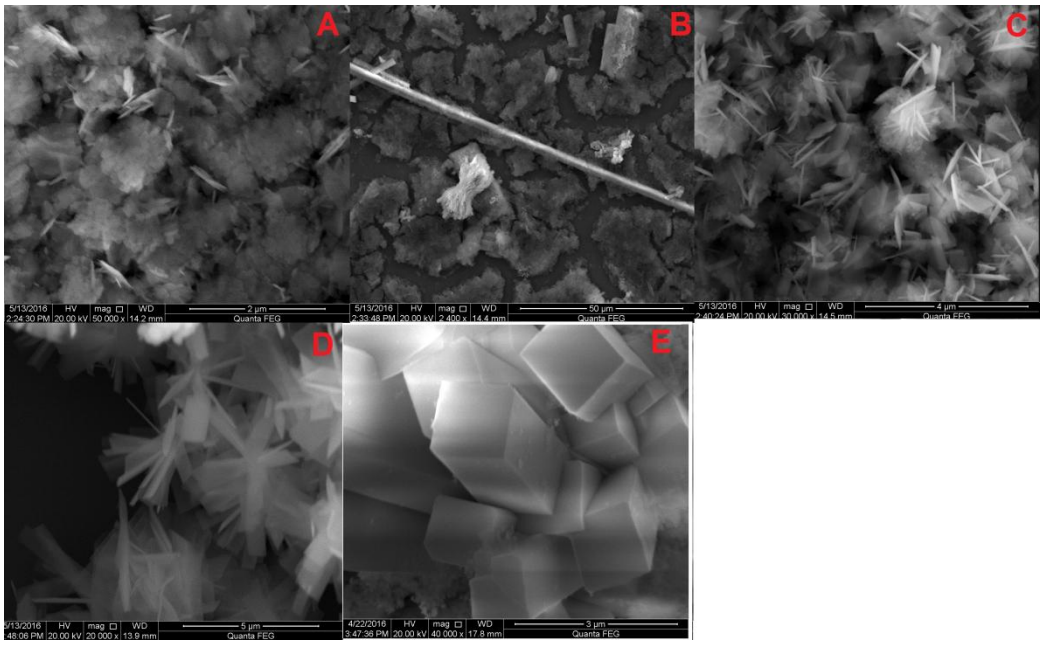

Figure 2.13 Scanning Electron Micrographs of Lithium Iron Phosphate Structures under several solvent conditions. (A-E) Ethylene glycol, Triton X-100, Glycerol, Diethylene Glycol, and water, respectively

Carbon Composite Studies

Figure 2.14 shows scanning electron micrographs of the lithium iron phosphate nanobelts after carbon coating. The web-like structure indicates successful pyrolysis of the sucrose precursor; however, the images also indicate a loss of homogeneity and elegance of the belt structures, as well as a poor degree of coating on the lithium iron phosphate itself. It would seem then that one of two phenomena occurred upon annealing: a large proportion of the material decomposed, or the belt structures are unstable under heat, and their aggregates fuse whereby the material develops a structure indistinguishable from what is typically produced via solid-state synthetic methods.[18]

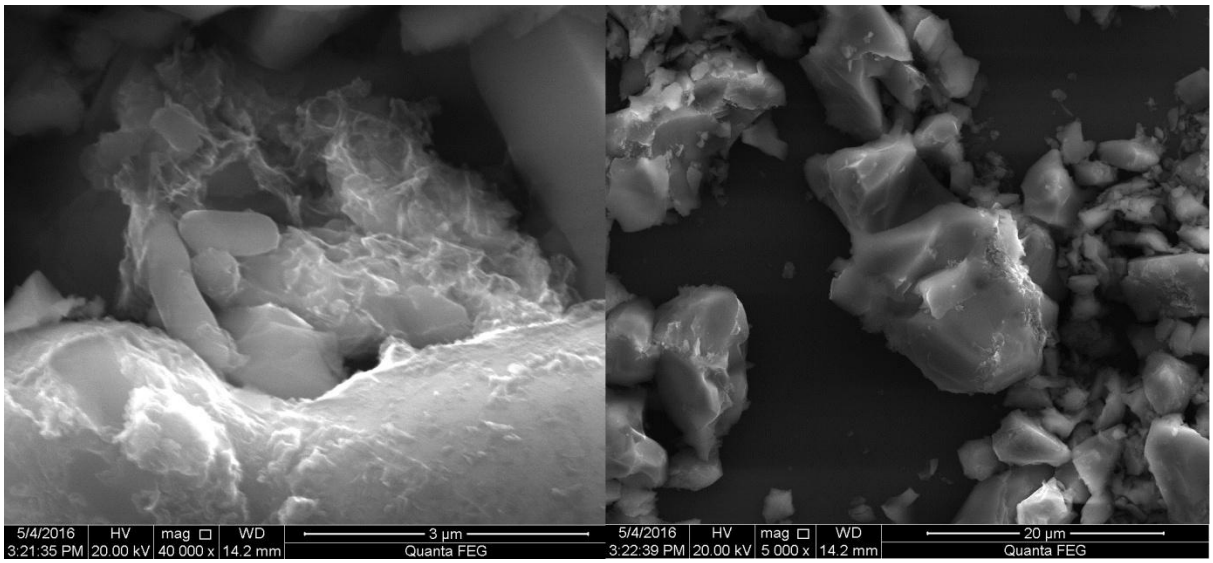

Figure 2.14 Scanning Electron Micrograph of Lithium Iron Phosphate nanobelts after annealing with sucrose dispersed upon the powder. It is noteworthy, that after doing so, not only is the coating quite heterogeneous, the material loses its previous morphology and takes on one not dissimilar from that produced by solid state reactions.

To perform as a pseudo-carbon coating, to wit, to create a conductive coating on the belts without the necessity of annealing, and to enhance ordering of the powder, pyridine-functionalized graphene (PyG) was produced. Figure 2.15 shows an FT-IR of graphene oxide before and after functionalization by a pyridinium salt reaction. The peak at 1420 cm^{-1} indicates the presence of a C-N bond.[47] A peak indicative of C=N, however, does not obviously appear, which may be a related to a poor degree of functionalization, where the peak is otherwise lost in the noise, or to that same end where the total signal is rather weak in and of itself. Additionally, as C=N signals undergo conjugation effects in IR, and as sites where pyridine would be functionalized are not identical in conjugation, the signal could be spread across several peaks that exhibit poor signal-to-noise.

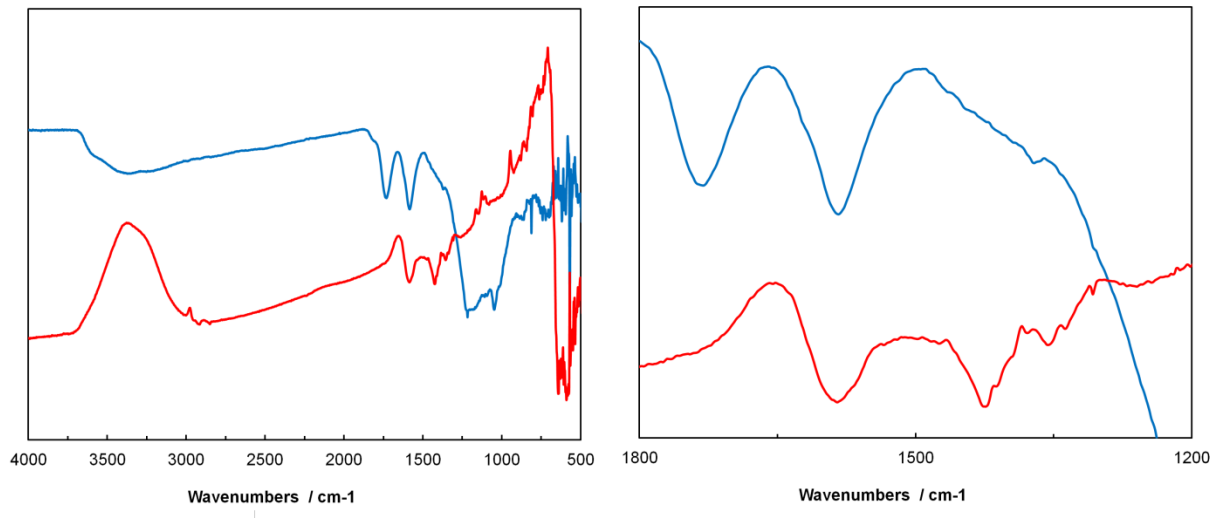

Figure 2.15 FT-IR of PyG, *red*, vs. graphene oxide, *blue*

Afterwards, PyG and LFP nanobelts were then sonicated together in ethanol to examine the aggregation of the respective materials. As seen from the SEM in Figure 2.16, the presence of PyG increases the incidence of aggregation in the sample, but does not tremendously help with ordering. This can be attributed to the non-homogeneity of the size and lamellarity of the PyG particles, whereby some are several fold larger than the LFP belts and some are considerably smaller; however, from the increased apparent surface roughness of the belts shown in the right micrograph from Figure 2.16, it would seem that the fewer layer sheets of PyG do adhere to the LFP belts, suggesting that the optimized form of this arrangement requires very few layer, or at least highly exfoliated PyG before combining with the LFP powder. Further, it is shown that the effect of long term sonication carries the risk of shattering the LFP belts, even under gentle bath sonication.

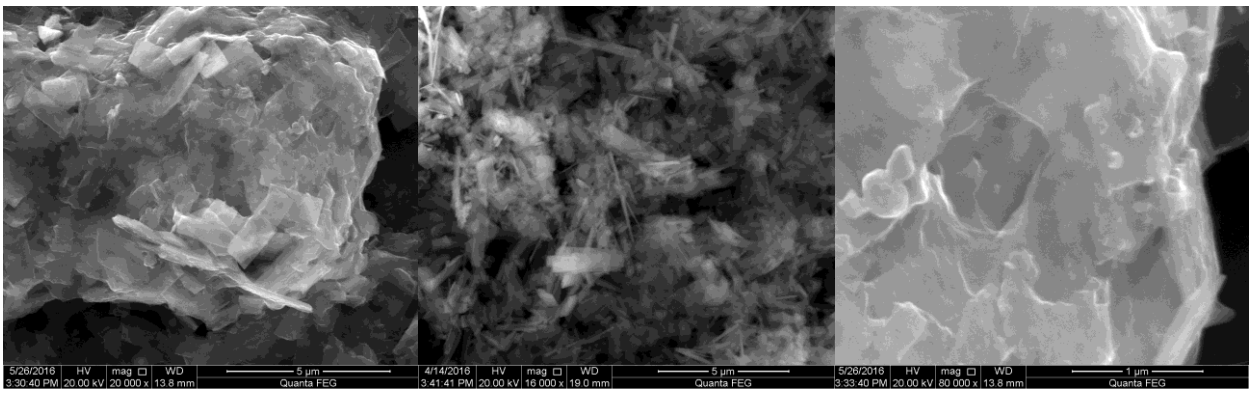

Figure 2.16 *Left:* Self-assembly of LFP nanobelts upon PyG with higher ordering after sonication to behave as a pseudo carbon coating relative to *Middle:* LFP nanobelts after sonication without PyG. *Right:* Further magnification of LFP/PyG composite

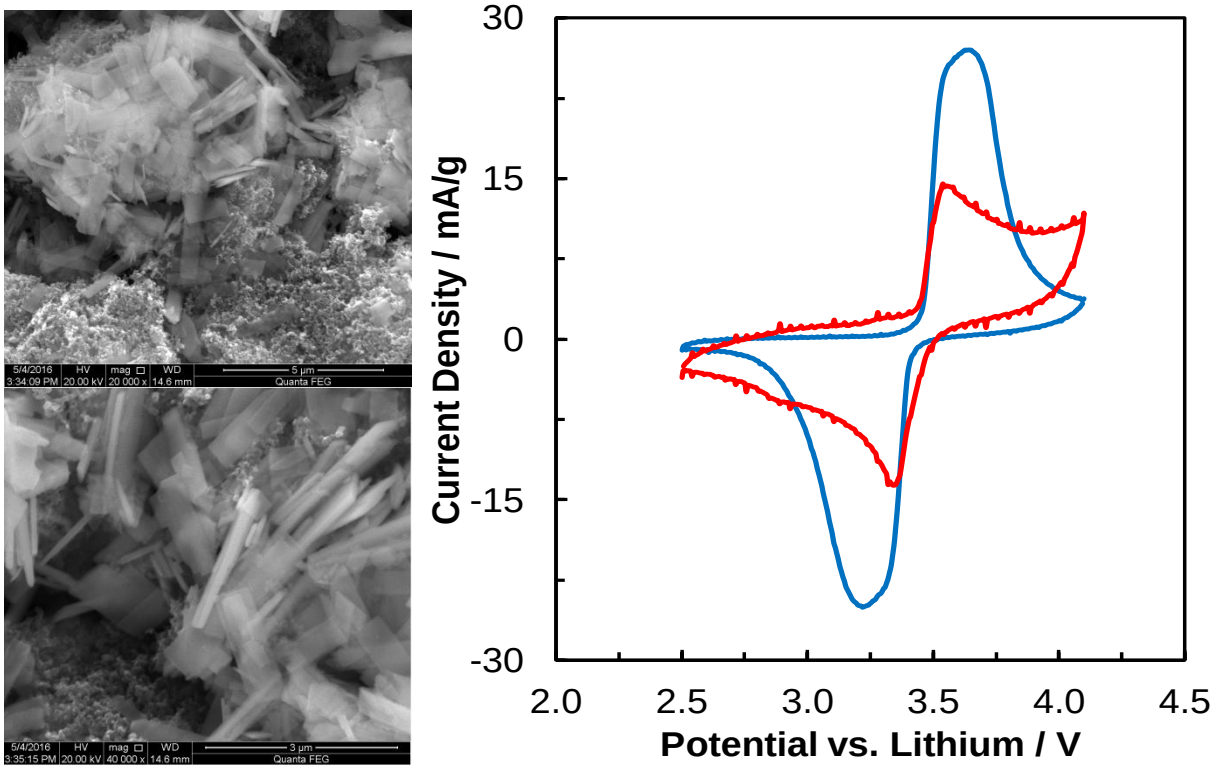

Figure 2.17 *Left:* Scanning Electron Micrographs of open coin cell after use. The smoothness of the material suggests no discernible degradation of the material due to cycling, nor from the electrolyte itself. *Right:* Cyclic voltammogram of the coin cell from the left, *red*, versus a commercial cell, *blue*. Of note is the lower onset potential for lithium removal, the narrowing of the difference in redox potentials.

As shown in the Figure 2.17 cyclic voltammograms, the lithium iron phosphate nanobelts exhibit reversible lithium intercalation. What is particularly relevant, however, is the lower onset potential for delithiation and lithiation of the material (meaning more negative on the oxidation sweep and more positive on the reduction sweep), as compared to the commercially available powder, even without the benefit of a conductive carbon coating. Furthermore, the material

exhibits a higher degree of potentiometric reversibility of the reaction as the peak potentials differentiate from the nominal voltage (~3.44 V with respect to Li/Li^+) less than does the commercial The oxidation and reduction peaks for commercial are 3.63 V and 3.22 V respectively. Likewise, the nanobelts are 3.54 V and 3.34 V, respectively. The implication of this is that the material requires, barring conductivity issues, less energy to remove lithium from the material and is more conducive to returning lithium ions to the material, implying the potential for a smaller net energy loss from the use of this material. Unfortunately, due to the morphology of the material, which is prone to self-assembly in lieu of its flat, smooth shape, the nanobelts have a propensity to aggregate in large masses of non-conductive lithium iron phosphate with mediocre contact between the belts and the carbon nanoparticles, as they would rather favor the contact between the belts themselves lending to a sort of "round peg in a square hole" problem, as shown in the micrographs in Figure 2.17. This connectivity and conductivity problem with the material and with the slurry itself corroborates the broadness of the peaks in the voltammogram, the higher capacitance of the material, as well as the inferior current density of the material relative to the commercial powder.

The cycling ability of the LFP nanobelts utilizing the pyridine-functionalized graphene as an additive was examined, and is shown in Figure 2.18. The materials were examined at 4 mA/g. The unaided lithiated 75.7% of its initial delithation, whereas the PyG composite retained 87.3%, showing that the composite either aided diffusion into the material, or alternatively, allowed reaction between the N groups and lithium ions.[52-54] Additionally, the initial voltage plateaus were unaffected by the PyG; however, its presence did present a prolonged lithium insertion and removal voltage plateau, capacity, and hysteresis on the LFP/PyG delithiation, notwithstanding.

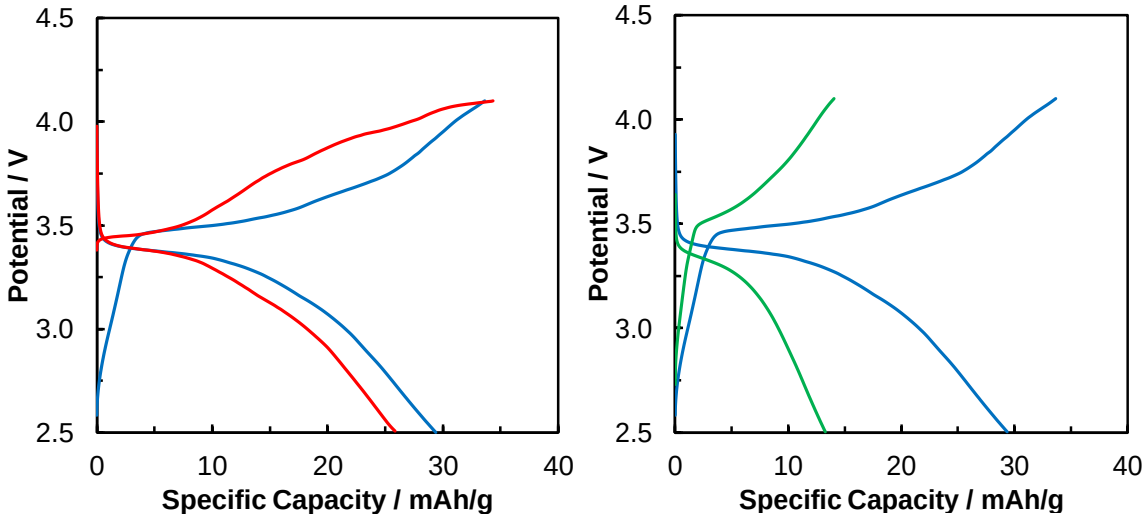

Figure 2.18 *Left:* Example of charge-discharge curves for LFP nanobelts with, *blue*, and without, *red*, PyG additive. Data is rendered as normalized to the delithiation capacity (charge) of the respective materials. *Right*: Charge-discharge curve for LFP/PyG composite at 4 mA/g, *blue*, and 20 mA/g, *green*.

Further, in Figure 2.18 on the right, shows a rate capability example for the LFP/PyG composite. The five-fold increase in current density begets an 80 mV shift for the voltage plateaus away from the average voltage for the reaction.

The efficacy of the pyridine-functionalized graphene composite was also examined by cyclic voltammetry, and is shown in Figure 2.19. The peaks for lithium insertion and removal are shifted by 54 mV; however, the current density, particularly for reinsertion of lithium increases by 25%. Further, in the case for both the charge-discharge curve and cyclic voltammogram for the unaided nanobelts, the respective unstable charge and increasing current density on the oxidative sweep, along with the noise, could be attributed to corrosion of the aluminum current collector as a result of a chloride impurity which are common with these syntheses.[55]

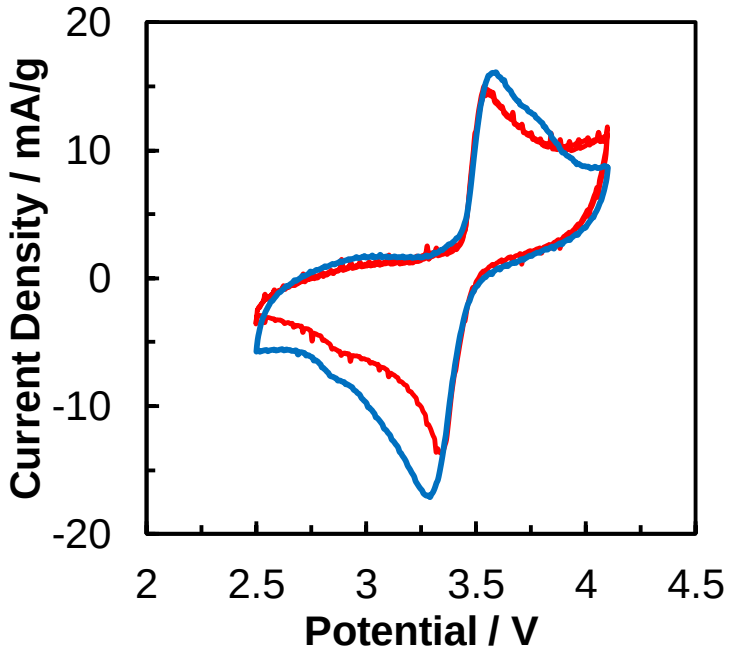

Figure 2.19 Cyclic voltammograms of LFP nanobelts with, *blue*, and without, *red*, PyG additive

Conclusions

In conclusion, lithium iron phosphate nanobelts were produced, as well as a myriad of other lithium iron phosphate morphologies. The effect of chloride content in the precursor, hydroxide content in the precursor, and solvent used were explored and discussed. The nanobelts unaided by any carbon-coating exhibit poor cycling, due to the inherent low conductivity of the material, as well as poor connectivity to the carbon additive in the coin cell. The synthesis and effect on aggregation of a new carbon additive was also explored and discussed.

CHAPTER 3

COPPER TITANTATE LITHIUM-ION BATTERY ELECTRODE

Introduction

The inception of the graphite anode in lithium-ion batteries allowed for the mass commercialization of lithium-ion batteries, which had previously been a litigious endeavor due to the risk of explosion caused by the use of lithium metal as the anode in rechargeable batteries. The novel anode afforded a large capacity of 372 mAh/g, and an intercalation voltage of ~60 mV. The advantage of this material stemmed from the intercalation voltage. Because of this ~60 mV above the potential for lithium deposition vs. lithium metal, the incidence of lithium dendrites were reduced at moderate charge rates. Despite this added safety and impressive capacity, however, relative to the demands of the modern market, the graphite anode is gradually coming up shorter and shorter.[56-57] Additionally, graphite itself is limited by the mechanism through which lithium intercalates into its structure. Upon attempted fast lithiation, lithium becomes deposited on the surface of the graphite, rather than intercalating, forming dendrites, and thus producing thermal runaway and possible explosion.[58]

Lithium titanium oxide spinel is a commercially available anode material for lithium-ion batteries. While its specific capacity (175 mAh/g) is less than the otherwise commercially applied graphite, its characteristics allow for superior efficacy at higher discharge rates, as well

as high durability due to the almost negligible volume change of the material.[59] The excellent rate capability extends from LTO's three-dimensional diffusion pathways from its spinel structure. Additionally, because of its low volume change, LTO typically has a high coulombic efficiency and can last up to 10,000 cycles.[6] Due to this limitation in capacity, which is only slightly higher than commercial cathode materials, however, studies in other anode materials have been made that can increase that capacity, decrease the cycling voltage, or increase the rate capability even further, or all three.[60-62] It generally follows that because the anode's capacity is much higher than the capacity of the cathode, full cells could be made by simply using more cathode material, and using less anode material to match that; however, in the case of LTO this is less practicable.

Other materials that attempt to address the weaknesses of graphite and LTO include metal oxides, silicon, and aluminum. Each of these materials have a substantially higher capacity than LTO and graphite, and a lithiation voltage lower than LTO.[61-64]

Silicon possesses a theoretical capacity of 3579 mAh/g and a lithiation voltage of 0.4 V.[64] Both of these capabilities are phenomenally valuable. The first places silicon's capacity competitively with lithium metal itself, and its voltage allows for a higher voltage full cell than the case with LTO.[65] The primary flaw of silicon, however, lies in its cycle life. Silicon, upon lithiation, expands in volume by three-fold. This expansion, after delithiation, causes severe degradation of the material and the silicon loses the ability to reintercalate lithium.[38, 66-68]

Copper oxide is another potential material for lithium-ion anodes. While it has a lower capacity than other metal oxide anodes due to its higher molar mass. It is environmentally benign and cheap. Additionally, it has a higher capacity than graphite: Cu_2O (375 mAh/) and CuO (674

mAh/g). The reaction with lithium ions and copper oxides produce lithium oxide and copper metal.[69-70] Copper (II) oxide cycles poorly, however, and tends to simply leave copper (I) oxide because the oxidation to +2 is inefficient.[71-74]

In the following sections a novel anodic copper oxide analogue material is described and its efficacy as an anode is explored.

Experimental

The copper titante powder was dried under vacuum for two hours at 120 °C. The powder was then combined in an 8:1 proportion by mass with Super-P carbon and ground together in an agate mortar. Afterwards, this powder was added to a solution of polyvinylidene difluoride (PVDF) in n-methyl pyrrolidone (NMP), whereby the concentration of PVDF constitutes an amount such that the final proportion by mass of the materials used are 8:1:1 active:carbon:PVDF. Additional NMP was subsequently added to the slurry to reduce the viscosity therein to the point of a flowing appearance of warm syrup. After homogenizing the slurry via stirring for a minimum of thirty minutes, it was then incrementally spread on an copper current collector foil, and then further spread to a uniform film by a doctor blade. Finally, the foil was dried under vacuum at 80 °C overnight, then pressed at 3000 psi.

The copper titanate anodes were tested via coin cell fabrication using CR 2032 coin cells from MTI Corporation. The electrolyte used was lithium hexaflurophosphate in a 1:1, by volume, solution of ethylene carbonate and diethylene carbonate. A schematic of the coin cell fabrication set up is shown in Figure 2.7.[33, 49]

To determine the working capacity of copper titanate as an anode material, a coin cell was subjected to a long and slow intercalation cycle. From that gravimetric capacity, the molar amount of lithiation that occurs could then be gleaned and a reaction for said intercalation could then be proposed. The data for this intercalation is given in Figure 3.1.

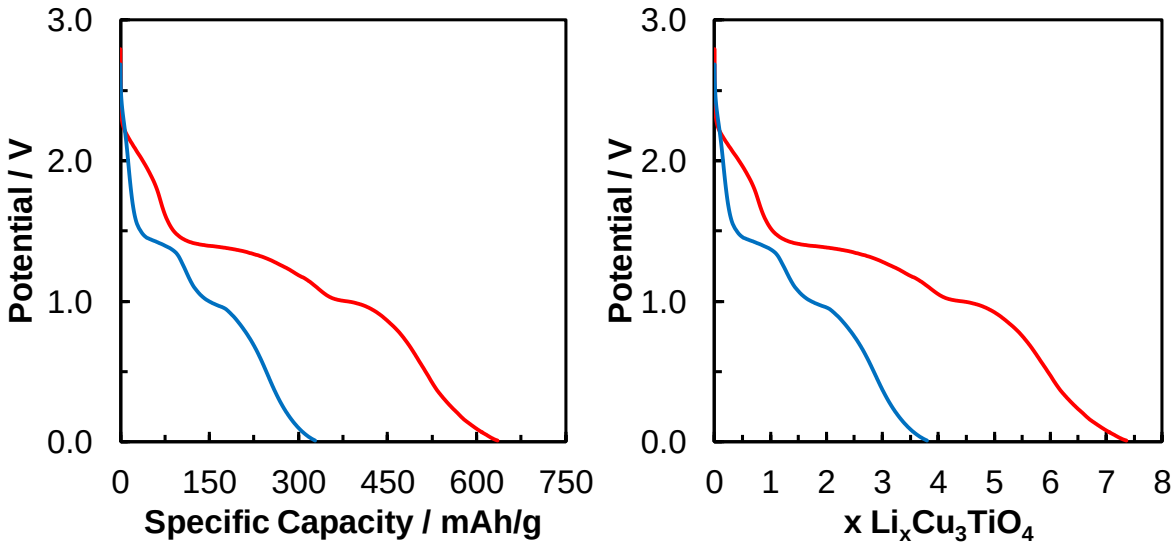

Figure 3.1 First (*red)* and second (*blue*) lithiation for Cu_3TiO_4. The calculation for the number of lithium ions into the material is given in Equation 3.1

From that gravimetric capacity (~635.8 mAh/g), the molar amount of lithiated into the anode could then be calculated, as shown in equation 3.1.

$$\mathbf{n} = \frac{\left(635.8\frac{\mathbf{mAh}}{\mathbf{g}} * 302.51\frac{\mathbf{g}}{\mathbf{mol}}\right)}{\frac{26800\ \mathbf{mAh}}{\mathbf{mol}}} = \mathbf{7.17} \quad (3.1)$$

Theoretically, however, the capacity of the material should be 531 mAh/g, corresponding to six lithium ions reacting with copper ions. The capacity beyond the sixth lithium corresponds to the formation of the SEI layer on the anode, as shown in Figure 3.3.[75] Further, from Figure 3.5, it follows that additional SEI layer is being formed on each cycle from the leveling out of the curve below 0.5 V. Additionally, it can be noted that the first plateau at 2 V disappears on the second lithiation. That plateau corresponds to the solid solution formed by lithium and the copper titanate (a copper oxide analogue), up to 0.4 Li/Cu. The second and third plateau correspond to the conversion of Cu (II) to Cu(0) and lithium oxide or lithium titanate.[75-77]

This is further corroborated by the cyclic voltammetry in Figure 3.2, wherein the solid solution formed by lithiation corresponds to 2 V (reduction peak) and 2.75 V (oxidation peak), respectively.[78-80] Like with Figure 3.1, the peak for that formation effectively disappears relative to the peaks for copper reduction.. The oxidation peaks of ~1.5 V and ~2.5 V correspond the subsequent return of copper to its oxidized species (copper titanate and copper oxide). The severe drop of current density between the first lithiation and subsequent cycles stems from two phenomena: the loss of copper to the electrolyte as dissolved species when converted to Cu^{+}, and large impetus needed to convert Cu^{+} to Cu^{+2} (~ 1.4V), and destruction of the crystal structure of the material as shown in the XRD from Figure 3.4.[81] Additionally, the drop in current beyond 0.5 V corresponds to the formation of the SEI layer.

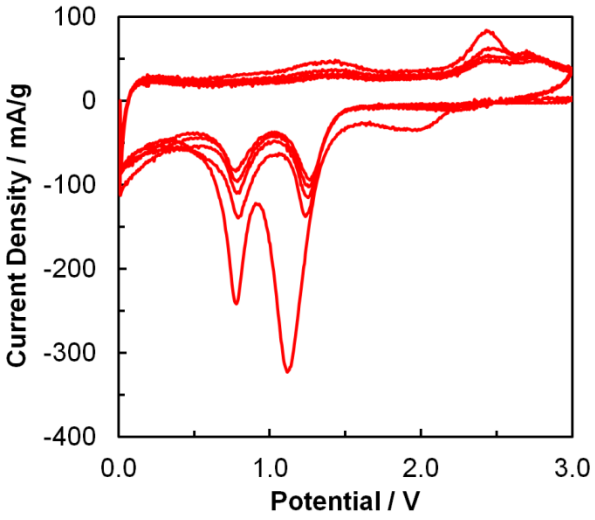

Figure 3.2 Cyclic voltammogram of copper titanate anode

The scanning electron micrographs from Figure 3.3 shows the formation of a smooth and thick surface-electrolyte-interface which is particularly valuable for the sake of conductivity and lithium transport. Further, despite the thickness of the SEI layer, the surface remains porous, which allows for maintaining homogeneous contact of the active material with the electrolyte.[82]

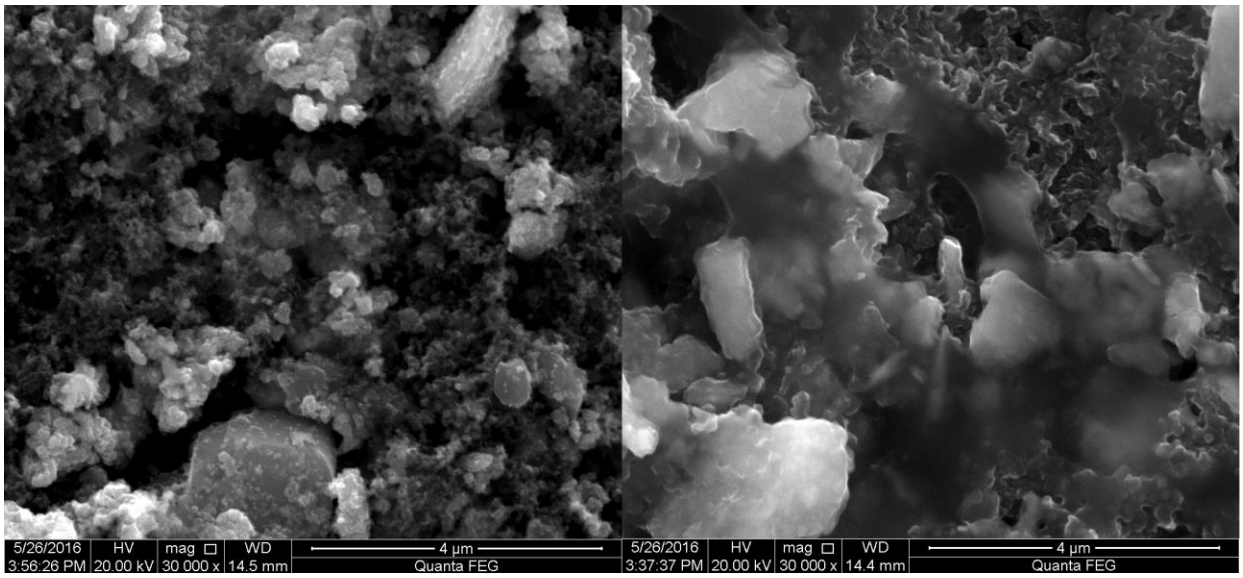

Figure 3.3 Scanning electron micrograph of copper titanate anode before and after cycling showing the formation of a thick and porous SEI layer

As shown from the X-ray diffraction patterns in Figure 3.4, the copper titanate anode undergoes a significant chemical change, and loss of crystallinity, over the course of cycling. Of note is the loss of the peak at 37.5°, and the peak at 36.5°, due to rutile-TiO_2 remains, partly due to the impurity in the original mixture.

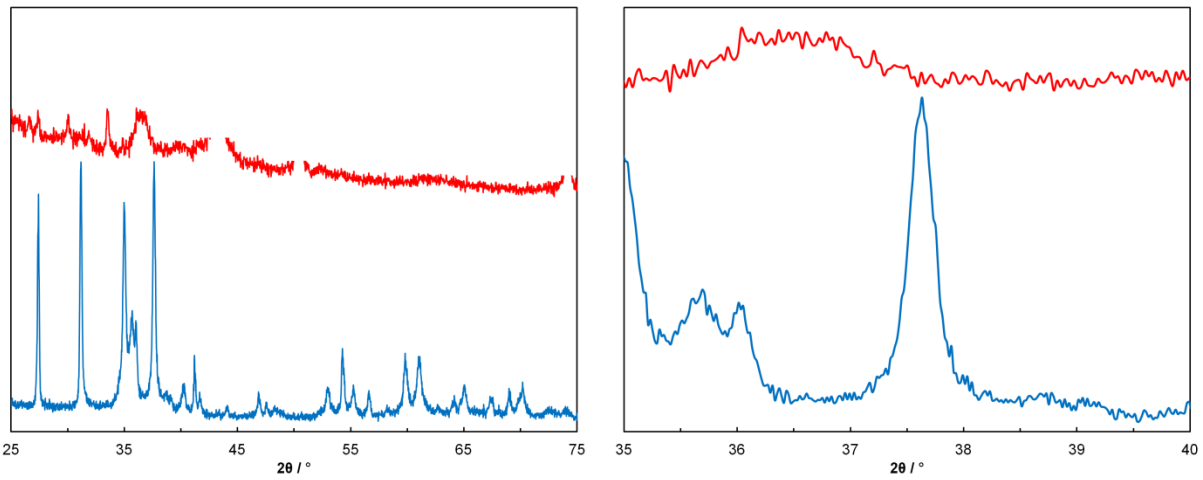

Figure 3.4 *Left:* X-ray Diffraction Pattern of Copper Titanate before, *blue*, and after, *red,* cycling over three hundred times. The gaps at 43, 50, and 74° peaks removed that are a product of copper metal in the current collector. *Right:* Magnification of peaks from 35°-40°

Also, the peak at 33.5°, indicates the presence of copper (II) oxide, likely stemming from the coin cell cycling being stopped during a partial delithiation, such that a small reconversion of the copper redox couple (partly responsible for the remaining meager capacity of the electrode) follows equation 3.2.

$$2CuO + 2Li^+ + 2e^- \rightarrow Cu_2O + Li_2O \quad (3.2)$$

$$Cu_2O + 2Li^+ + 2e^- \rightarrow 2Cu + Li_2O \quad (3.3)$$

In Figure 3.5, the charge and discharge performance of the copper titanate anodes is demonstrated. The material over several cycles shows a drastic loss of capacity from the loss of the ability to utilize the copper redox couples in the material. Additionally, the plateaus

corresponding to the copper couples effectively disappear, with a very faint exception with the conversion of a faint plateau for the copper couple.

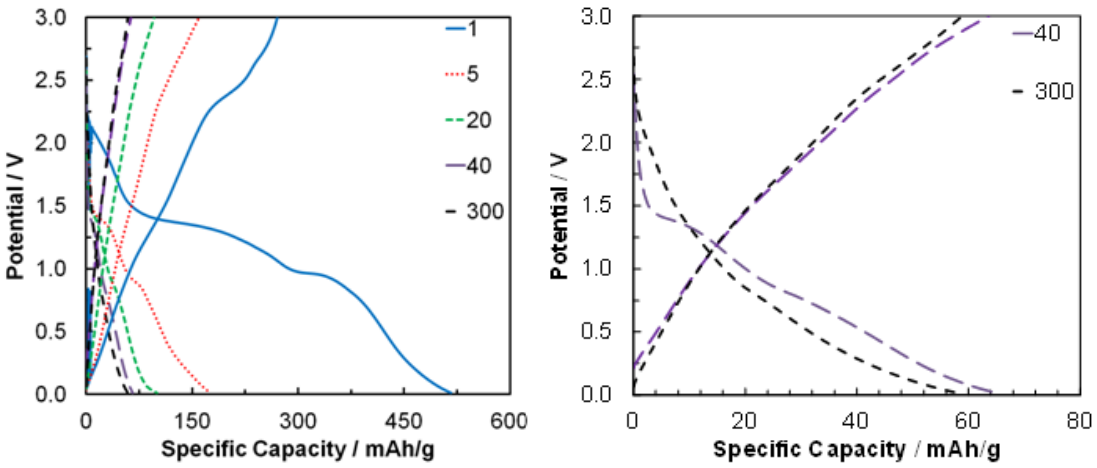

Figure 3.5 *Left:* Long-term charge/discharge curves for copper titanate anode collected at 20 mA/g *Right:* Fortieth and Three-hundredth charge/discharge curves

Additionally, in Figure 3.6, is shown the efficacy of the material over the course of 400 cycles. As previously discussed, the material undergoes precipitous capacity fade; however, it becomes steady at ~60 mAh/g, with a coulombic efficiency of ~99.6%.

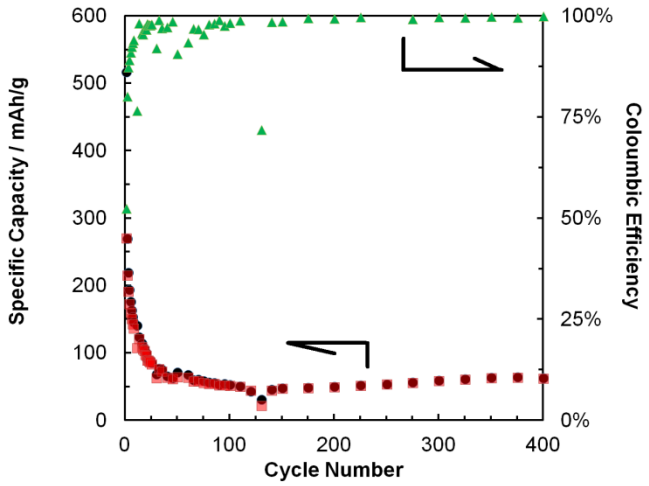

Figure 3.6 Long-term cycling data for copper titanate, recorded at 20 mA/g from 3-0.1V

Finally, rate studies were also performed on the copper titanate electrodes, as seen in Figure 3.7. The coulombic efficiency remained steady except in the case where the current density was changed, and maintained an average of 99.7%.

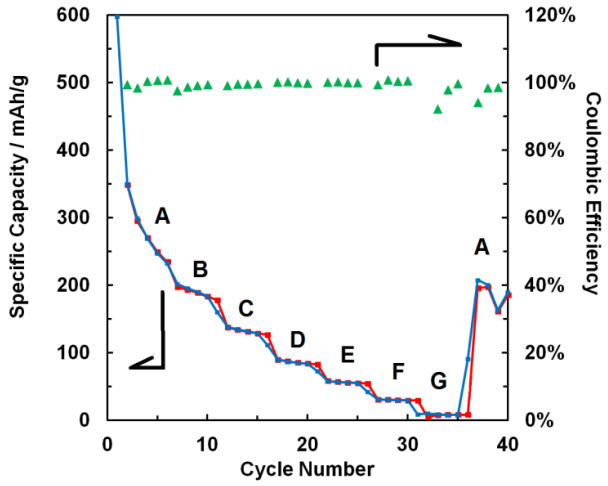

Figure 3.7 *Left:* Rate capability for copper titanate anode **A-G:** 30, 60, 120, 300, 600, 1200, 3000 mA/g, respectively. Green represents coulombic efficiency, blue represents lithiation, and red represents delithiation.

Conclusions

In conclusion, a novel anode material for lithium-ion batteries was presented. The material demonstrated a high specific capacity with three voltage plateaus at 2 V, 1.4 V, and 1 V, wherein the bulk of which was at the latter two plateaus. Unfortunately, the material exhibits poor cycle life and poor rate capability due to loss of copper to the electrolyte and structural degradation from intercalation.

CHAPTER 4

INDIRECT DETECTION OF CHOLESTEROL WITH MOLECULARLY-TETHERED CHOLESTEROL OXIDASE

Introduction

Hypercholesterolemia, an excess of blood serum cholesterol, carries a 100% increase in risk of atherosclerosis when levels are twenty percent above the average adult cholesterol concentration (200 mg/dL). The profile for blood cholesterol is subdivided as such: high density lipids (HDL), low density lipids (LDL), and triglycerides. HDL cholesterol is the vehicle through which previously deposited cholesterol is moved from blood vessel walls, and is thus considered the "good" cholesterol. Conversely, LDL is considered to be the "bad" cholesterol responsible for clogged arteries and the like.[83-84] High density lipid cholesterol levels below 40 mg/dL are considered detrimental and above 60 mg/dL are considered to help prevent cardiovascular disease, whereas LDL below 100 mg/dL is considered favorable and above 190 mg/dL is considered extremely detrimental.[85] Indeed, in the majority of tests for blood cholesterol, particularly for those with hypercholesterolemia, familial or otherwise, will be for LDL.

The modified Abell-Kendall method is the most robust method known for testing blood cholesterol. To wit, serum samples are treated with potassium hydroxide in alcohol and incubated for nearly one hour, then cooled, extracted by centrifugation into ether, dried, and

subsequently treated with a Liebermann-Burchard reagent, a reagent incorporating acetic anhydride, such that, upon reaction with cholesterol a green color is produced and measured via colorimetry.[86,87] As the protocol may suggest, a substantial amount of time, equipment, and laboratory expertise is needed, which necessitates a likewise substantial cost for utilizing such a screening method.

Another, oft used in clinics, is performed by automated analyzers. The use of these instruments lie in their ability to perform several of other blood tests, in addition to determining cholesterol levels. Unfortunately, however, their performance is limited by the abilities of clinic using the device, which can lead to error. In spite of this, they are preferred by clinics due to the speed and number of tests they can perform.[87]

Enzymatic Electron Transfer

Indirect Electron Transfer

The first generation of biosensors utilize indirect detection of their respective analytes. Indirect detection, or indirect electron transfer, as it will be referred to herein for consistency with subsequent sections, is the process whereby the primary analyte of interest is detected through the reaction of a secondary species on the electrode surface. It differs from mediated electron transfer in two respects: the first, it is not recycled by the electrode/enzyme system, and second it utilizes a natural co-substrate of the enzyme. For example, in the case of FAD enzymes, such as cholesterol oxidase, as outlined in equations 4.1-4.3, the natural co-substrate of the enzyme for the oxidation reaction of the FAD couple is oxygen.[88] As such, the method through which this

reaction is utilized requires the use of oxygen at the electrode surface (equation 4.4), the disproportionation reaction of hydrogen peroxide at the electrode surface, or a bienzyme system where hydrogen peroxide, for example, catalyzes the latter.[89-90]

$$\text{holesterol} + O_2 \xrightarrow{\text{ChOx}} \text{Cholest} - 4 - \text{en} - \text{one} + H_2O_2 \quad (4.1)$$

$$\text{hOx(FAD)} + 2e^- + 2H^+ \leftrightarrow \text{hOx}(FADH_2) \quad (4.2)$$

$$\text{hOx}(FADH_2) + O_2 \rightarrow \text{hOx(FAD)} + H_2O_2 \quad (4.3)$$

$$O_2 + 2e^- + 2H^+ \rightarrow H_2O \quad (4.4)$$

A schematic of indirect electron transfer is given in Figure 4.1.

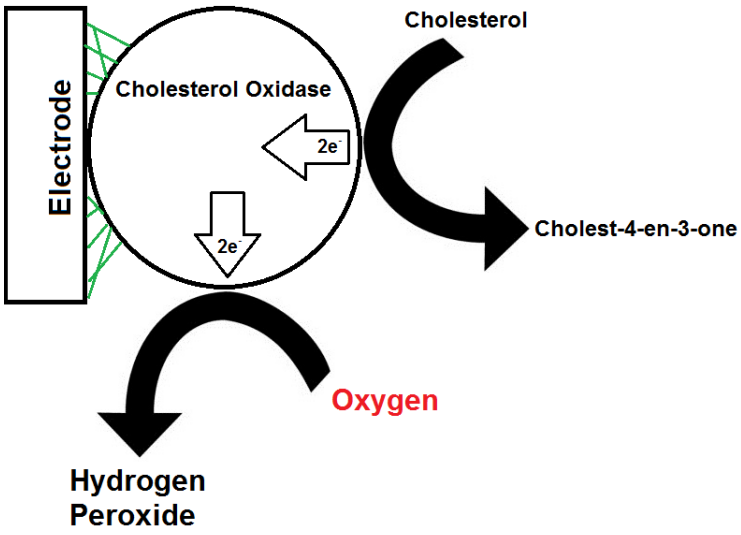

Figure 4.1 Schematic of Indirect Detection Mechanism of Cholesterol with Cholesterol Oxidase in a Single-Enzyme System. Oxygen (red) is the analyte of interest.[89]

Mediated Electron Transfer

Mediated electron transfer employs the redox couple of a secondary reagent to shuttle electrons from the redox couple in an enzyme to the electrode. This is particularly useful in the common case where detection is by direct response of the enzyme cofactor is impossible due to distance of the cofactor from the electrode, as well as the orientation, and denaturing of the enzyme when immobilized at the electrode surface.[91-94] A schematic of this mechanism with cholesterol oxidase as an example is given in Figure 4.2.

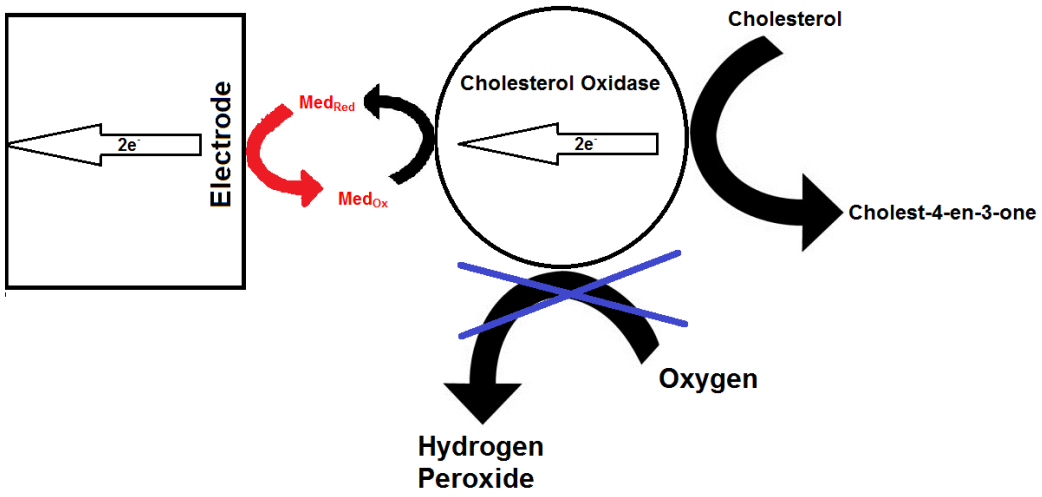

Figure 4.2 Schematic of Mediated Electron Transfer reaction of Cholesterol with Cholesterol Oxidase. The oxidation of the mediator reduced by $FADH_2$ is the reaction of interest (Red). The blue X indicates the reaction is done without the presence of oxygen in solution, or that the reaction of the mediator has greater affinity for scavenging electrons from the FAD cofactor.

Direct Electron Transfer

Direct electron transfer, or direct detection, focuses on the detection of an analyte by the oxidation or reduction of an analyte by an electrode functionalized by a catalyst. This method entails utilizing a redox couple from the catalyst used, or the redox couple of the analyte itself, when applicable. Figure 4.1 demonstrates a schematic whereby cholesterol would theoretically be detected via direct electron transfer. The proton and electron transfer takes place at the enzyme cofactor, in this case flavin adenine dinucleotide (FAD). In order to detect this reaction, the electrons given to the cofactor have to then be drawn to the electrode. To accomplish this, the co-substrate of the reaction, oxygen, removed from the reaction, as it would otherwise be reduced to hydrogen peroxide.[95] This is an arduous response to detect due to the distance of the well buried cofactor from the electrode, as well as the orientation, and denaturing of the enzyme when immobilized at the electrode surface.[91-94]

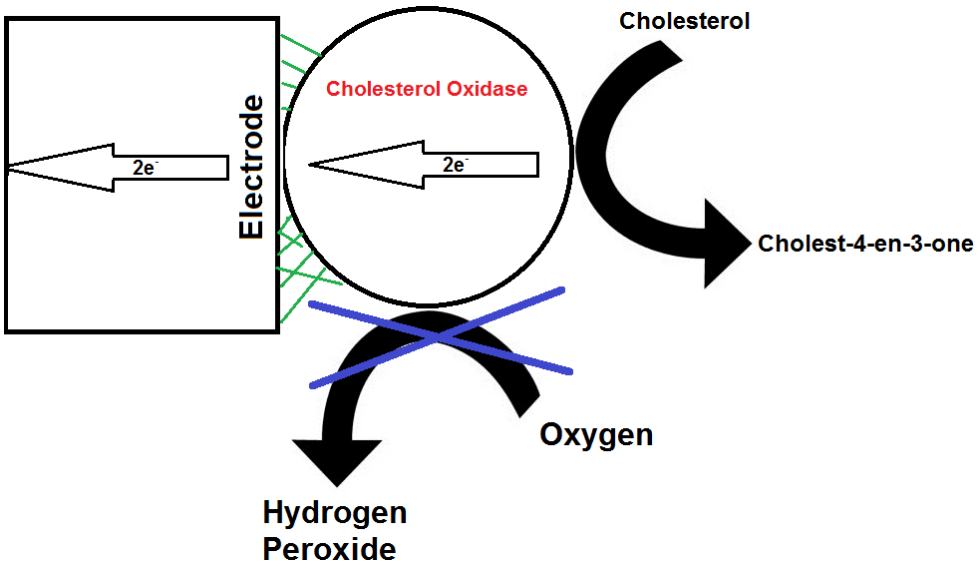

Figure 4.3 Schematic of Direct Detection reaction of Cholesterol with Cholesterol Oxidase. The redox couple of the FAD/$FADH_2$ cofactor is the reaction of interest, particularly the oxidation reaction of $FADH_2$ to FAD. The reaction is such that the electrode has superior affinity for scavenging electrons from the cofactor compared to oxygen, or that oxygen is removed from the system, thus it is shown to be excluded.

Immobilization Methods and Enzyme Specificity

To maximize the enzyme/substrate interactions occurring near the electrode surface, and to maximize the rate of diffusion of substrate to the electrode surface, the enzyme is commonly immobilized at the electrode surface. This can be accomplished by film deposition, molecular tethering, covalent crosslinking, and other methods.[89, 96-98]

The enzymatic biosensor owes a great deal of its precision for detecting its analyte of interest to the specificity of enzymes to their substrates. This is particularly important to medical sensors where blood contains a cocktail of biomolecules and as such the specificity of an enzyme.[99-100]

Applications

The first enzymatic biosensor was developed by Leland Clark and Ann Lyons utilizing glucose oxidase on an oxygen, or Clark, electrode.[101] Since that time, the enzymatic glucose meter has been ubiquitous method of facile glucose monitoring.

In addition to biosensors, or rather in tandem with biosensors, enzymes can be used to produce a "self-powering" biosensor such that the sensor operates like a fuel cell, where the analyte is the fuel source as well.[102]

In the following sections, a first generation biosensor based on cholesterol oxidase is demonstrated and its efficacy in cholesterol detection and specificity against common interferents is demonstrated.[89]

Experimental

Materials Preparation

Multi-walled carbon nanotubes were suspended in dimethylformamide by sonication in a concentration of 1 mg/mL. 10 mM PBSE was prepared by dissolving PBSE in DMF.

Cholesterol suspensions were prepared by dissolving 38.6 mg of cholesterol in 0.5 mL isopropanol and 0.5 mL Triton X-100. Subsequently, the solution was diluted with 100 mM pH 7.4 sodium phosphate buffer to 10 mL to yield 10 mM cholesterol stock.

Acetaminophen tablets were weighed and powdered then dissolved in 100 mM pH 7.4 sodium phosphate buffer to yield 84.7 mM solution. Solid uric acid was dissolved in 10 mL 4 mM sodium hydroxide to yield 2.4 mM stock. Sodium lactate and glucose solids were dissolved in the 100 mM buffer for 10 mM and 2 M stocks, respectively.

Immobilization of Cholesterol Oxidase

The electrodes were prepared as described previously.[96] To wit, a glassy carbon electrode was polished with alumina powder followed by sonication in distilled water, followed by ethanol. Then, the electrode was dried at 80°C. Six microliters of the nanotube suspension was dropcast onto the electrode surface in two microliter increments drying at 80°C between each. After this, the electrode was then put on ice.

The PBSE tethering solution (5 μL) was dropcast on the electrode. The solution was left to react with the nanotube coating for thirty minutes on ice before being rinsed with DMF to remove unreacted PBSE, followed by 20 mM pH 7.4 sodium phosphate buffer, to wet the electrode surface for immobilization of the enzyme respectively such that the enzyme would not be shocked by the change in solvent.

Then, 5 μL of cholesterol oxidase stock solution was dropcast onto the electrode and left on ice for thirty minutes so that the enzyme could react with the PBSE and be tethered to the electrode surface via pi-pi stacking at the pyrene/nanotube interface, and by covalent attachment the reaction of the primary amines in the enzyme to the NHS ester in the PBSE.[96] After incubation, the electrode was rinsed with 20 mM pH 7.4 sodium phosphate buffer to remove unimmobilized enzyme.

Electrochemical Characterization

Electrochemical characterizations were performed on a glassy carbon electrode, with an Ag/AgCl reference electrode (0.197 V vs. NHE), and a platinum counter electrode as shown in the schematic in Figure 4.4. Experiments were performed using the Model 1040C Multi-Potentiostat (CH Instruments).

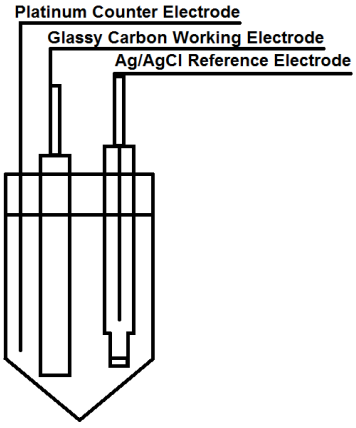

Figure 4.4 Schematic of electrochemical cell for testing cholesterol oxidase functionalized electrodes

Results and Discussion

Electrode Characterization

The electrode was characterized by cyclic voltammetry in nitrogen saturated 100 mM pH 7.4 sodium phosphate buffer. As per Figure 4.5 A, immobilization of the enzyme was carried out successfully. The curve with cholesterol oxidase immobilized on the electrode shows a distinct peak corresponding to the FAD/$FADH_2$ redox couple. In the instance where the enzyme was not functionalized on the electrode, no such peak occurred.[103] Indeed, when compared to a case where no PBSE was used and the enzyme was dropcast and "immobilized" by physisorption, Figure 4.5 B, no such discernible peak appears. This suggests that the enzyme was successfully immobilized and in superior loading of the enzyme relative to physisorption.

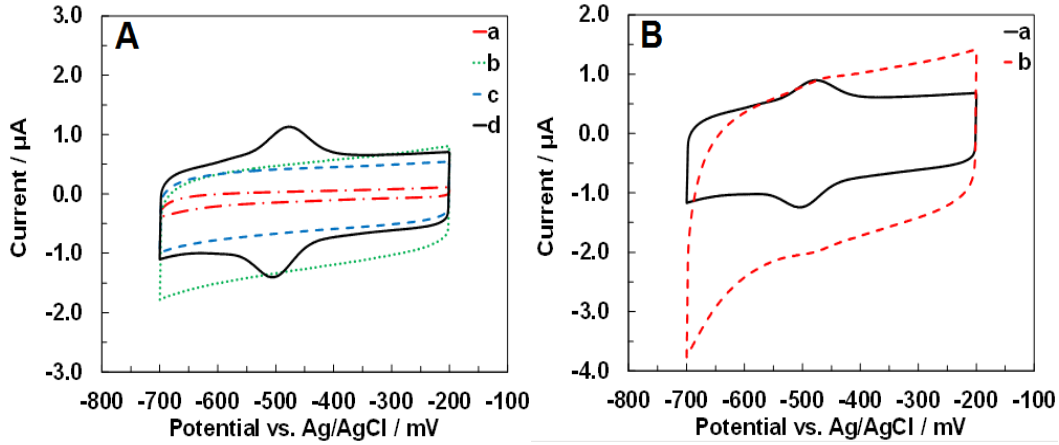

Figure 4.5 (**A**) Immobilization control experiments (a) bare glassy carbon electrode, (b) MWCNT/GC, (c) PBSE/MWCNT/GC, and (d) ChOx/PBSE/MWCNT/GC electrode. (**B**) Immobilization comparison of PBSE-immobilized ChOx electrode (a) and Physisorbed Cholesterol Oxidase electrode (b). *Scan rate: 10 mV/s*

To determine the optimum pH for the study of this reaction cyclic voltammetry at several pHs of phosphate buffer was performed. The pH for all subsequent studies was chosen for three reasons: First, physiological pH is 7.4, the pH of blood. Second, the ideal biological pH for cholesterol oxidase activity is 7.0. Third, the optimized electrochemical pH for this enzyme was determined to be 7.5 as it has the greatest cathodic activity for the enzyme, as shown in Figure 4.6. In lieu of this information, the physiological pH was chosen, because it is practical and near the three pH values mentioned. Additionally, the correlation between pH and formal potential is given in Figure 4.6. The slope therein was -59.9 mV/pH, corresponding to a one electron per proton transfer.[104]

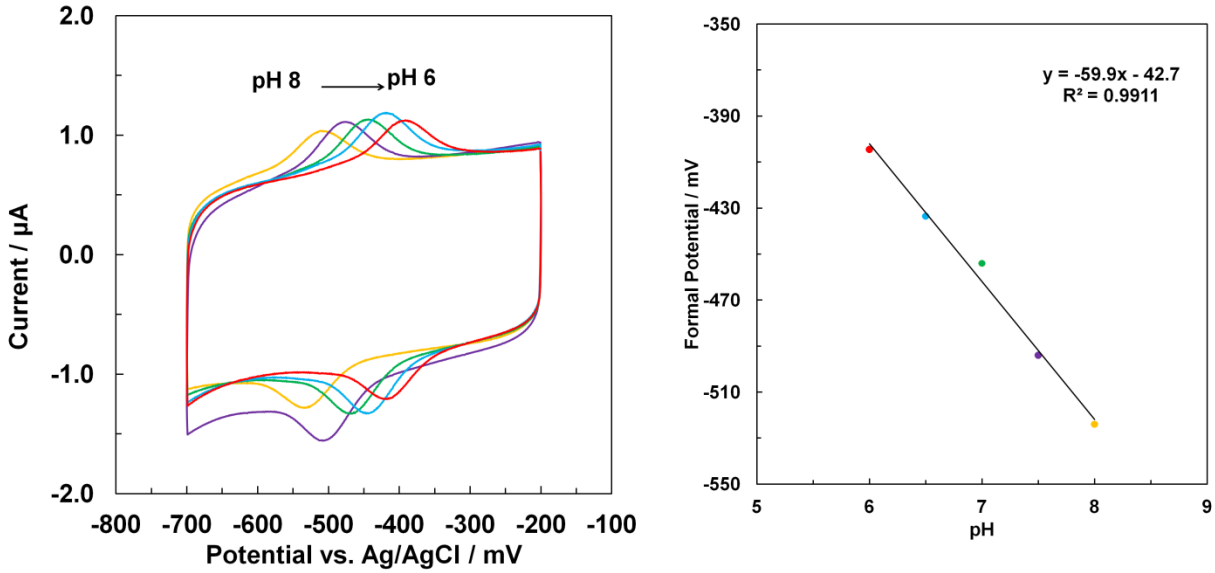

Figure 4.6 *Left:* pH study of ChOx biosensor *Right:* Trend of the formal potential versus pH

The scan rate was also varied to examine the reversibility of the FAD/$FADH_2$ redox couple. Cyclic voltammetry was conducted at scan rates from 10 to 500 mV/s. As shown in Figure 4.7, the deviation current versus scan rate is only 9.8 nA/mV/s. Thus, the electrode exhibits good reversibility for the redox couple. Further, the peak voltage for the couple doesnt vary much below 200 mV/s; however, beyond that they both shift linearly with the log of the scan rate.

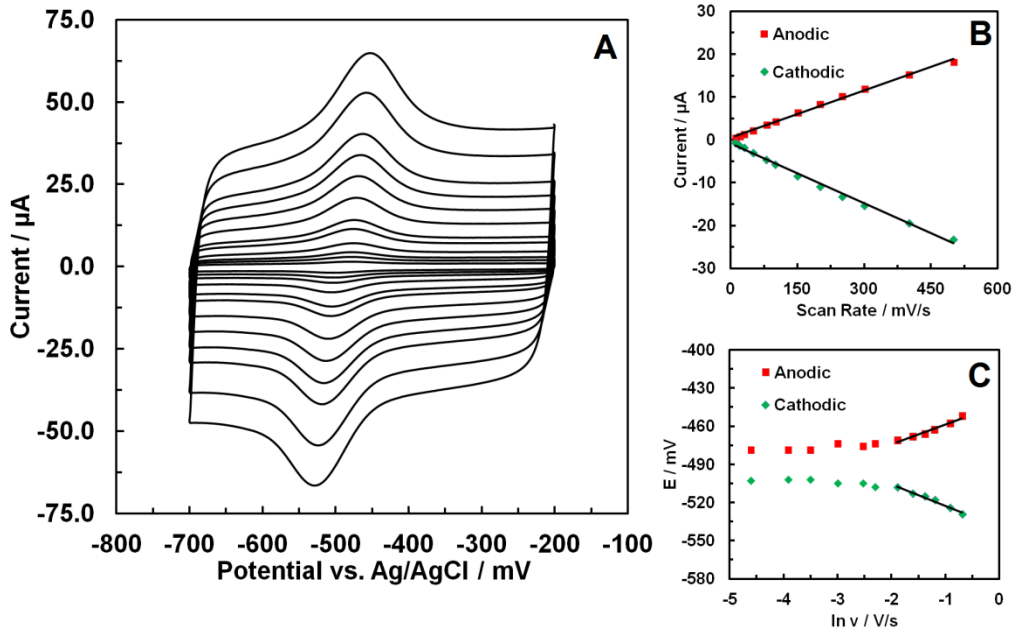

Figure 4.7 Scan rate study of ChOx biosensor **A:** CV thereof. Increasing current corresponds to 10, 20, 30, 50, 80, 100, 150, 200, 250, 300, 400, and 500 mV/s respectively. **B:** Peak current vs. Scan rate for peak, where the slopes are 36.9 nA/mV/s for the anodic and -46.7 nA/mV/s for the cathodic trend lines. **C:** Peak potential vs. log of scan rate

Cholesterol Detection

The sensor's detection efficacy was examined with cyclic voltammetry and differential pulse voltammetry. Figure 4.8 shows the sensor responses to the addition of cholesterol on the concentration of oxygen at the electrode surface and, by extension, in the bulk. A concentration curve was generated from the decrease in the peak current from differential pulse voltammetry at -475 mV, which was due to the consumption of oxygen by the immobilized enzyme from the reaction.

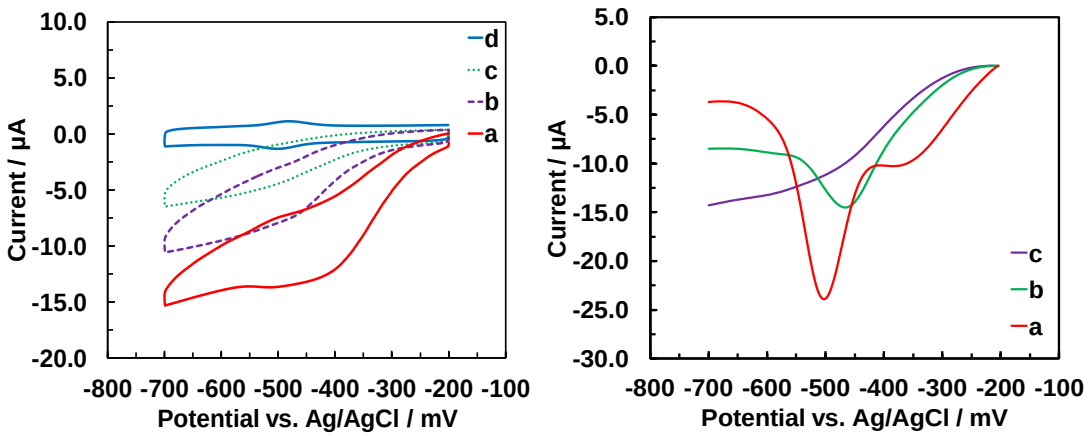

Figure 4.8 *Left*: Cyclic Voltammograms of ChOx immobilized on MWCNT via PBSE crosslinker (a) 0 mM cholesterol, (b) 0.5 mM cholesterol, and (c) 1.0 mM cholesterol. (d) is the absence of oxygen and cholesterol; *Right:* Differential Pulse Voltammograms of ChOx/PBSE/MWCNT/GC electrode. a, b, and c are under the same conditions as the left.

The concentration curve for the sensor and a comparison to selected literature values are shown in Figure 4.9 and TABLE I, respectively. The linear region for the sensor was determined to be

from 0.5 μM to 8 μM with a correlation of 0.9915. As the typical blood concentration of cholesterol is one-thousand-fold higher than this, the sensor shows a fair degree of practicality relative to necessary sample size, especially when considering the amount of electrolyte that would be used in a commercial biosensor relative to our working electrolyte volume (5 mL). The linear region sensitivity was 0.6061 μA/μM. From the Haines-Woolf plot rendered from this data, the $K_m^{apparent}$ and V_{max} were determined to be 1.14 μM and 12.407 μA^{-1}, respectively.

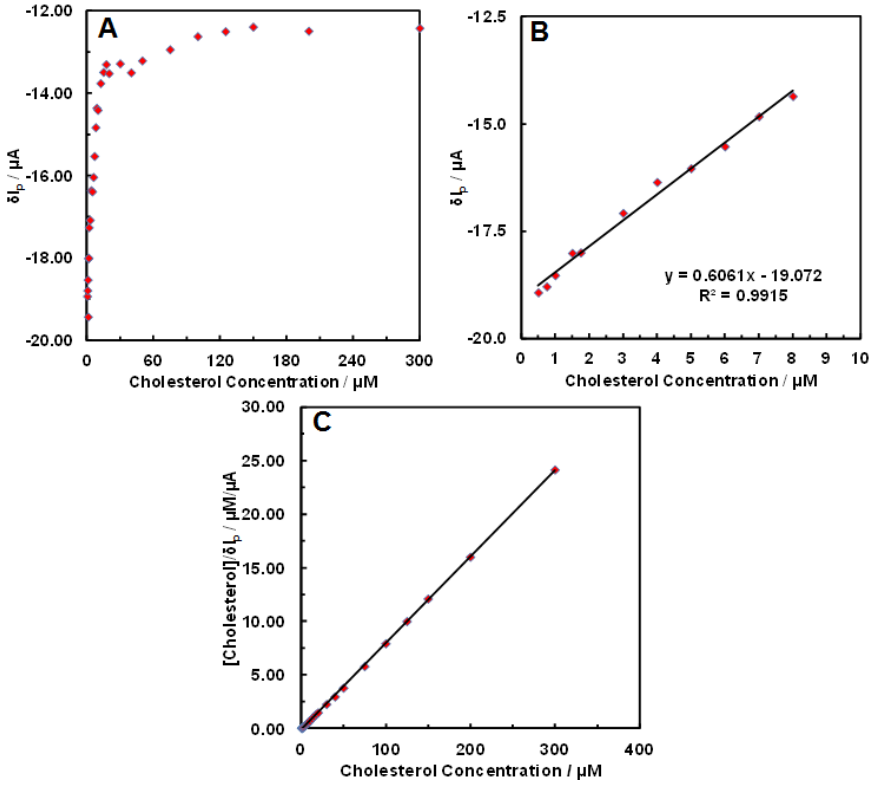

Figure 4.9 Concentration Data for PBSE-immobilized Cholesterol Oxidase **A:** Concentration of cholesterol versus the peak current from the differential pulse voltammetry data. **B:** Expansion of the linear region rendered from **A**. **C:** Haines-Woolf Plot of the same data

TABLE I. Efficacy of Biosensor from Figure 4.9 vs. Selected Literature Values

Electrode	$K_m^{apparent}$	Linear Range	Source
ChOx/PtPd-CS-GS/GCE	110 μM	8.8-12.2 mM	(105)
ChOx/MEH-PPV/SA	----------	1290-12910 μM	(106)
ChOx/Nano-CdS/ITO	220 μM	5-1300 μM	(107)
ChOx/CS-GR/GCE	17.39 μM	5-1000 μM	(104)
GCE/PTH/ChOx/HRP	----------	25-125 μM	(108)
ChOx/PBSE/MWCNT/GCE	1.14 μM	0.5-8 μM	(89)

Interference Studies

Differential pulse voltammetry was used to determine the selectivity of the biosensor against common interfering agents found in blood.[104, 109] The concentration of the interferents were presented at double the concentration of cholesterol. As such, the concentrations were presented in tremendous physiological excess, as shown in the Effective Concentration column in TABLE II.[110-113] The change in current from 5 μM cholesterol concentration was 10.8%, -1.9%, 11.7 %, and 5.2% for glucose, acetaminophen, uric acid, and sodium lactate, respectively. The sensor showed acceptable selectivity for cholesterol oxidation via oxygen reduction loss, even at severe excess of interferents.

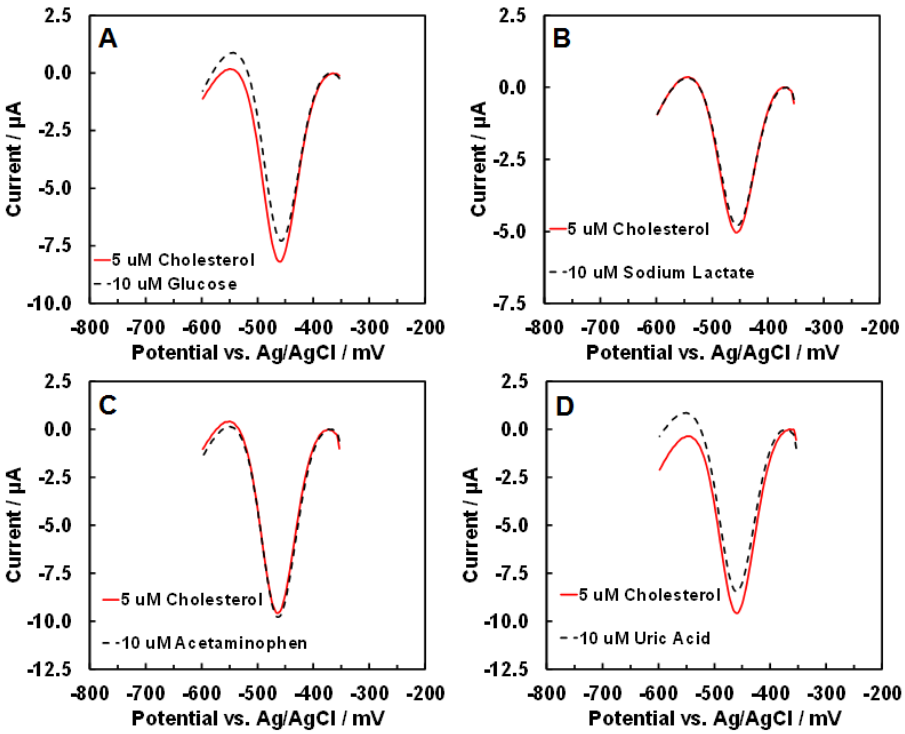

Figure 4.10 Interference Data for PBSE-immobilized Cholesterol Oxidase. (**A**-**D**) Differential Pulse Voltammogram for Glucose, Sodium Lactate, Acetaminophen, and Uric Acid.

TABLE II. Interference Values From Figure 4.10

Interfering Agent	Typical Physiological Concentration	Effective Concentration	Current Deviation vs. 5 µM Cholesterol
10 µM Glucose	4.4-6.1 mM	8.8-12.2 mM	10.8%
10 µM Acetaminophen	66.2-165.4 µM	8.2-20.5 M	-1.9%
10 µM Uric Acid	202-416 µM	8.1-16.6 mM	11.7%
10 µM Sodium Lactate	1- >20 mM	0.6 mM-> 8.2 M	5.2%

Conclusions

In conclusion, a cholesterol biosensor was developed utilizing the indirect detection of cholesterol via the detection of the loss of oxygen available for reduction at the electrode surface due to the reaction of cholesterol oxidase with cholesterol. The enzyme was immobilized by molecular tethering of multiwall carbon nanotubes with PBSE. The linear range was 0.5-8 μM, and the sensor demonstrated robust selectivity in the presence of common interfering agents.

CHAPTER 5

CONCLUSIONS

To conclude, what was demonstrated were studies of the morphologies formed of lithium iron phosphate by subtle tweaks to the precursor. The changes in hydroxide content in the precursor seemed to have the most profound effect on the morphology, likely due in part to changing the iron precursor from iron (ii) chloride to iron (ii) hydroxide. With solvents, the ones that possessed three oxygen containing groups under the conditions optimized to one produced nanobelts, whereas the others produced a variety of shapes. Chloride ions didn't seem to have a distinct effect on the morphology of the material produced beyond a certain threshold. The lithium iron phosphate nanobelts were then functionalized with pyridine-functionalized graphene to behave as a pseudo-carbon coating for improved cyclability.

Additionally, the efficacy of a novel anode material, copper titanate, was explored. The anode exhibited impressive capacity; however, it suffered greatly on continued cycling and at higher rates.

Finally, a cholesterol oxidase biosensor was discussed. The sensor exhibited a high degree of sensitivity with a linear range broad enough to cover the physiological limits of humans, but using a 1/1000th dilution of sample. In addition to that, the sensor showed little interference, even against physiologically impossible concentrations of interfering agents.

REFERENCES

1. Heller, A., Electrochemical cell. Google Patents: 1975.

2. Whittingham, M. S., Electrical Energy Storage and Intercalation Chemistry. *Science* **1976,** *192* (4244), 1126-1127.

3. Mizushima, K.; Jones, P. C.; Wiseman, P. J.; Goodenough, J. B., LixCoO2 (0<x<-1): A new cathode material for batteries of high energy density. *Materials Research Bulletin* **1980,** *15* (6), 783-789.

4. Harry, K. J.; Hallinan, D. T.; Parkinson, D. Y.; MacDowell, A. A.; Balsara, N. P., Detection of subsurface structures underneath dendrites formed on cycled lithium metal electrodes. *Nat Mater* **2014,** *13* (1), 69-73.

5. Teki, R.; Datta, M. K.; Krishnan, R.; Parker, T. C.; Lu, T.-M.; Kumta, P. N.; Koratkar, N., Nanostructured Silicon Anodes for Lithium Ion Rechargeable Batteries. *Small* **2009,** *5* (20), 2236-2242.

6. Buchmann, I., *Batteries in a Portable World: A Handbook on Rechargeable Batteries for Non-Engineers, Third Edition*. 3 ed.; Cadex Electronics Inc.: 2011.

7. Buqa, H.; Goers, D.; Holzapfel, M.; Spahr, M. E.; Novák, P., High Rate Capability of Graphite Negative Electrodes for Lithium-Ion Batteries. *Journal of The Electrochemical Society* **2005,** *152* (2), A474-A481.

8. Buhrmester, C.; Moshurchak, L.; Wang, R. L.; Dahn, J. R., Phenothiazine Molecules: Possible Redox Shuttle Additives for Chemical Overcharge and Overdischarge Protection for Lithium-Ion Batteries. *Journal of The Electrochemical Society* **2006,** *153* (2), A288-A294.

9. Hamenu, L.; Lee, H. S.; Latifatu, M.; Kim, K. M.; Park, J.; Baek, Y. G.; Ko, J. M.; Kaner, R. B., Lithium-silica nanosalt as a low-temperature electrolyte additive for lithium-ion batteries. *Current Applied Physics* **2016,** *16* (6), 611-617.

10. Wang, Z.; Xing, L.; Li, J.; Xu, M.; Li, W., Triethylborate as an electrolyte additive for high voltage layered lithium nickel cobalt manganese oxide cathode of lithium ion battery. *Journal of Power Sources* **2016,** *307*, 587-592.

11. Qi, X.; Tao, L.; Hahn, H.; Schultz, C.; Gallus, D. R.; Cao, X.; Nowak, S.; Roser, S.; Li, J.; Cekic-Laskovic, I.; Rad, B. R.; Winter, M., Lifetime limit of tris(trimethylsilyl) phosphite as electrolyte additive for high voltage lithium ion batteries. *RSC Advances* **2016,** *6* (44), 38342-38349.

12. Tran-Van, F.; Provencher, M.; Choquette, Y.; Delabouglise, D., Dihydrophenazine derivatives for overcharge protection of rechargeable lithium batteries. *Electrochimica Acta* **1999,** *44* (16), 2789-2792.

13. Yin, X.; Huang, K.; Liu, S.; Wang, H.; Wang, H., Preparation and characterization of Na-doped LiFePO4/C composites as cathode materials for lithium-ion batteries. *Journal of Power Sources* **2010,** *195* (13), 4308-4312.

14. Park, S. H.; Shin, S. S.; Sun, Y. K., The effects of Na doping on performance of layered Li1.1 − xNax[Ni0.2Co0.3Mn0.4]O2 materials for lithium secondary batteries. *Materials Chemistry and Physics* **2006,** *95* (2–3), 218-221.

15. Ouyang, C.-Y.; Wang, D.-Y.; Shi, S.-Q.; Wang, Z.-X.; Li, H.; Huang, X.-J.; Chen, L.-Q., First Principles Study on Na x Li 1− x FePO 4 As Cathode Material for Rechargeable Lithium Batteries. *Chinese Physics Letters* **2006,** *23* (1), 61.

16. Ouyang, C. Y.; Shi, S. Q.; Wang, Z. X.; Li, H.; Huang, X. J.; Chen, L. Q., The effect of Cr doping on Li ion diffusion in LiFePO 4 from first principles investigations and Monte Carlo simulations. *Journal of Physics: Condensed Matter* **2004,** *16* (13), 2265.

17. Yang, L.; Jiao, L.; Miao, Y.; Yuan, H., Improvement of electrochemical properties of LiFePO4/C cathode materials by chlorine doping. *Journal of Solid State Electrochemistry* **2009,** *13* (10), 1541-1544.

18. Wang, J.; Sun, X., Understanding and recent development of carbon coating on LiFePO4 cathode materials for lithium-ion batteries. *Energy & Environmental Science* **2012,** *5* (1), 5163-5185.

19. Liao, X.-Z.; He, Y.-S.; Ma, Z.-F.; Zhang, X.-M.; Wang, L., Effects of fluorine-substitution on the electrochemical behavior of LiFePO4/C cathode materials. *Journal of Power Sources* **2007,** *174* (2), 720-725.

20. Croce, F.; D' Epifanio, A.; Hassoun, J.; Deptula, A.; Olczac, T.; Scrosati, B., A Novel Concept for the Synthesis of an Improved LiFePO4 Lithium Battery Cathode. *Electrochemical and Solid-State Letters* **2002,** *5* (3), A47-A50.

21. Li, H.; Zhou, H., Enhancing the performances of Li-ion batteries by carbon-coating: present and future. *Chemical Communications* **2012,** *48* (9), 1201-1217.

22. Tian, N.; Gao, Y.; Li, Y.; Wang, Z.; Song, X.; Chen, L., Li2C2, a High-Capacity Cathode Material for Lithium Ion Batteries. *Angewandte Chemie International Edition* **2016,** *55* (2), 644-648.

23. Gibot, P.; Casas-Cabanas, M.; Laffont, L.; Levasseur, S.; Carlach, P.; Hamelet, S.; Tarascon, J. M.; Masquelier, C., *Nat. Mater*. **2008,** *7*, 741.

24. Wilcox, J. D.; Doeff, M. M.; Marcinek, M.; Kostecki, R., Factors Influencing the Quality of Carbon Coatings on LiFePO4. *Journal of The Electrochemical Society* **2007,** *154* (5), A389-A395.

25. Doeff, M. M.; Wilcox, J. D.; Kostecki, R.; Lau, G., Optimization of Carbon Coatings on LiFePO4. *Journal Name: Journal of Power Sources; Journal Volume: 163; Journal Issue: 1SI; Related Information: Journal Publication Date: 12/07/2006* **2005**, Medium: ED.

26. Goodenough, J. B.; Kim, Y., Challenges for Rechargeable Li Batteries. *Chemistry of Materials* **2010,** *22* (3), 587-603.

27. Sun, Y. K.; Han, J. M.; Myung, S. T.; Lee, S. W.; Amine, K., Significant improvement of high voltage cycling behavior AlF3-coated LiCoO2 cathode. *Electrochemistry Communications* **2006,** *8* (5), 821-826.

28. Chung, S.-Y.; Bloking, J. T.; Chiang, Y.-M., Electronically conductive phospho-olivines as lithium storage electrodes. *Nat Mater* **2002,** *1* (2), 123-128.

29. Delacourt, C.; Poizot, P.; Tarascon, J.-M.; Masquelier, C., The existence of a temperature-driven solid solution in LixFePO4 for 0 [le] x [le] 1. *Nat Mater* **2005,** *4* (3), 254-260.

30. Ravet, N.; Abouimrane, A.; Armand, M., From our readers: On the electronic conductivity of phospho-olivines as lithium storage electrodes. *Nat Mater* **2003,** *2* (11), 702-702.

31. Ellis, B. L.; Makahnouk, W. R. M.; Makimura, Y.; Toghill, K.; Nazar, L. F., A multifunctional 3.5[thinsp]V iron-based phosphate cathode for rechargeable batteries. *Nat Mater* **2007,** *6* (10), 749-753.

32. Guo, B.; Ruan, H.; Zheng, C.; Fei, H.; Wei, M., Hierarchical LiFePO4 with a controllable growth of the (010) facet for lithium-ion batteries. *Scientific Reports* **2013,** *3*, 2788.

33. Julien, C.; Mauger, A.; Vijh, A.; Zaghib, K., Lithium Batteries. In *Lithium Batteries*, Springer International Publishing: 2016; pp 29-68.

34. Aravindan, V.; Gnanaraj, J.; Lee, Y.-S.; Madhavi, S., LiMnPO4 - A next generation cathode material for lithium-ion batteries. *Journal of Materials Chemistry A* **2013,** *1* (11), 3518-3539.

35. Islam, M. S.; Driscoll, D. J.; Fisher, C. A. J.; Slater, P. R., Atomic-Scale Investigation of Defects, Dopants, and Lithium Transport in the LiFePO4 Olivine-Type Battery Material. *Chemistry of Materials* **2005,** *17* (20), 5085-5092.

36. Morgan, D.; Van der Ven, A.; Ceder, G., Li Conductivity in Li x MPO 4 (M = Mn , Fe , Co , Ni) Olivine Materials. *Electrochemical and Solid-State Letters* **2004,** *7* (2), A30-A32.

37. Nishimura, S.-i.; Kobayashi, G.; Ohoyama, K.; Kanno, R.; Yashima, M.; Yamada, A., Experimental visualization of lithium diffusion in LixFePO4. *Nat Mater* **2008,** *7* (9), 707-711.

38. Kang, B.; Ceder, G., Battery materials for ultrafast charging and discharging. *Nature* **2009,** *458* (7235), 190-193.

39. Chen, D. P.; Maljuk, A.; Lin, C. T., Floating zone growth of lithium iron (II) phosphate single crystals. *Journal of Crystal Growth* **2005,** *284* (1–2), 86-90.

40. Malik, R.; Abdellahi, A.; Ceder, G., A Critical Review of the Li Insertion Mechanisms in LiFePO4 Electrodes. *Journal of The Electrochemical Society* **2013,** *160* (5), A3179-A3197.

41. Guo, L.; Zhang, Y.; Wang, J.; Ma, L.; Ma, S.; Zhang, Y.; Wang, E.; Bi, Y.; Wang, D.; McKee, W. C.; Xu, Y.; Chen, J.; Zhang, Q.; Nan, C.; Gu, L.; Bruce, P. G.; Peng, Z., Unlocking the energy capabilities of micron-sized LiFePO(4). *Nature Communications* **2015,** *6*, 7898.

42. Dominko, R.; Gaberscek, M.; Drofenik, J.; Bele, M.; Pejovnik, S.; Jamnik, J., The role of carbon black distribution in cathodes for Li ion batteries. *Journal of Power Sources* **2003,** *119–121*, 770-773.

43. Malik, R.; Burch, D.; Bazant, M.; Ceder, G., Particle Size Dependence of the Ionic Diffusivity. *Nano Letters* **2010,** *10* (10), 4123-4127.

44. Gaberscek, M.; Dominko, R.; Jamnik, J., Is small particle size more important than carbon coating? An example study on LiFePO4 cathodes. *Electrochemistry Communications* **2007,** *9* (12), 2778-2783.

45. Delacourt, C.; Poizot, P.; Levasseur, S.; Masquelier, C., Size Effects on Carbon-Free LiFePO4 Powders: The Key to Superior Energy Density. *Electrochemical and Solid-State Letters* **2006,** *9* (7), A352-A355.

46. Zhao, Y.; Peng, L.; Liu, B.; Yu, G., Single-Crystalline LiFePO4 Nanosheets for High-Rate Li-Ion Batteries. *Nano Letters* **2014,** *14* (5), 2849-2853.

47. Verma, S.; Kumar, S.; Shawat, E.; Nessim, G. D.; Jain, S. L., Carbon nanofibers decorated with oxo–rhenium complexes: Highly efficient heterogeneous catalyst for oxidation of amines with hydrogen peroxide. *Journal of Molecular Catalysis A: Chemical* **2015,** *402*, 46-52.

48. Bayazit, M. K.; Clarke, L. S.; Coleman, K. S.; Clarke, N., Pyridine-Functionalized Single-Walled Carbon Nanotubes as Gelators for Poly(acrylic acid) Hydrogels. *Journal of the American Chemical Society* **2010,** *132* (44), 15814-15819.

49. Kayyar, A.; Huang, J.; Samiee, M.; Luo, J., Construction and testing of coin cells of lithium ion batteries. *Journal of visualized experiments : JoVE* **2012,** (66), e4104.

50. Zhou, N.; Wang, H.-Y.; Uchaker, E.; Zhang, M.; Liu, S.-Q.; Liu, Y.-N.; Cao, G., Additive-free solvothermal synthesis and Li-ion intercalation properties of dumbbell-shaped LiFePO4/C mesocrystals. *Journal of Power Sources* **2013,** *239*, 103-110.

51. Dokko, K.; Koizumi, S.; Nakano, H.; Kanamura, K., Particle morphology, crystal orientation, and electrochemical reactivity of LiFePO4 synthesized by the hydrothermal method at 443 K. *Journal of Materials Chemistry* **2007,** *17* (45), 4803-4810.

52. Qie, L.; Yuan, L.-X.; Zhang, W.-X.; Chen, W.-M.; Huang, Y.-H., Revisit of Polypyrrole as Cathode Material for Lithium-Ion Battery. *Journal of The Electrochemical Society* **2012,** *159* (10), A1624-A1629.

53. Huang, Y.-H.; Park, K.-S.; Goodenough, J. B., Improving Lithium Batteries by Tethering Carbon-Coated LiFePO4 to Polypyrrole. *Journal of The Electrochemical Society* **2006,** *153* (12), A2282-A2286.

54. Wang, G. X.; Yang, L.; Chen, Y.; Wang, J. Z.; Bewlay, S.; Liu, H. K., An investigation of polypyrrole-LiFePO4 composite cathode materials for lithium-ion batteries. *Electrochimica Acta* **2005,** *50* (24), 4649-4654.

55. Popovic, J.; Demir-Cakan, R.; Tornow, J.; Morcrette, M.; Su, D. S.; Schlögl, R.; Antonietti, M.; Titirici, M.-M., LiFePO4 Mesocrystals for Lithium-Ion Batteries. *Small* **2011,** *7* (8), 1127-1135.

56. Liu, B.; Wang, X.; Chen, H.; Wang, Z.; Chen, D.; Cheng, Y.-B.; Zhou, C.; Shen, G., Hierarchical silicon nanowires-carbon textiles matrix as a binder-free anode for high-performance advanced lithium-ion batteries. *Scientific Reports* **2013,** *3*, 1622.

57. Jia, H.; Gao, P.; Yang, J.; Wang, J.; Nuli, Y.; Yang, Z., Novel Three-Dimensional Mesoporous Silicon for High Power Lithium-Ion Battery Anode Material. *Advanced Energy Materials* **2011,** *1* (6), 1036-1039.

58. Evarts, E. C., Lithium batteries: To the limits of lithium. *Nature* **2015,** *526* (7575), S93-S95.

59. Kurc, B.; Swiderska-Mocek, A., Properties of Li4Ti5O12 as an anode material in non-flammable electrolytes. *Journal of Applied Electrochemistry* **2013,** *44* (2), 245-253.

60. Tang, H.; Zan, L.; Zhu, J.; Ma, Y.; Zhao, N.; Tang, Z., High rate capacity nanocomposite lanthanum oxide coated lithium zinc titanate anode for rechargeable lithium-ion battery. *Journal of Alloys and Compounds* **2016,** *667*, 82-90.

61. Li, S.; Niu, J.; Zhao, Y. C.; So, K. P.; Wang, C.; Wang, C. A.; Li, J., High-rate aluminium yolk-shell nanoparticle anode for Li-ion battery with long cycle life and ultrahigh capacity. *Nat Commun* **2015,** *6*.

62. Chen, P.; Wu, F.; Wang, Y., Four-Layer Tin–Carbon Nanotube Yolk–Shell Materials for High-Performance Lithium-Ion Batteries. *ChemSusChem* **2014,** *7* (5), 1407-1414.

63. Yu, S.-H.; Lee, S. H.; Lee, D. J.; Sung, Y.-E.; Hyeon, T., Conversion Reaction-Based Oxide Nanomaterials for Lithium Ion Battery Anodes. *Small* **2016,** *12* (16), 2146-2172.

64. Polat, B. D.; Keles, O., Designing self-standing silicon-copper composite helices as anodes for lithium ion batteries. *Journal of Alloys and Compounds* **2016,** *677*, 228-236.

65. Rohan, J. F.; Hasan, M.; Patil, S.; Casey, D. P.; Clancy, T., *ICT - Energy - Concepts Towards Zero - Power Information and Communication Technology*. InTech: 2014.

66. Wang, C.; Wu, H.; Chen, Z.; McDowell, M. T.; Cui, Y.; Bao, Z., Self-healing chemistry enables the stable operation of silicon microparticle anodes for high-energy lithium-ion batteries. *Nat Chem* **2013,** *5* (12), 1042-1048.

67. Besenhard, J. O.; Yang, J.; Winter, M., Will advanced lithium-alloy anodes have a chance in lithium-ion batteries? *Journal of Power Sources* **1997,** *68* (1), 87-90.

68. Arico, A. S.; Bruce, P.; Scrosati, B.; Tarascon, J.-M.; van Schalkwijk, W., Nanostructured materials for advanced energy conversion and storage devices. *Nat Mater* **2005,** *4* (5), 366-377.

69. Ikeda, H.; Narukawa, S., Behaviour of various cathode materials for non-aqueous lithium cells. *Journal of Power Sources* **1983,** *9* (3), 329-334.

70. Grugeon, S.; Laruelle, S.; Herrera-Urbina, R.; Dupont, L.; Poizot, P.; Tarascon, J.-M., Particle Size Effects on the Electrochemical Performance of Copper Oxides toward Lithium. *Journal of The Electrochemical Society* **2001,** *148* (4), A285-A292.

71. Morales, J.; Sánchez, L.; Bijani, S.; Martínez, L.; Gabás, M.; Ramos-Barrado, J. R., Electrodeposition of Cu2 O ： An Excellent Method for Obtaining Films of Controlled Morphology and Good Performance in Li-Ion Batteries. *Electrochemical and Solid-State Letters* **2005,** *8* (3), A159-A162.

72. Zhang, C. Q.; Tu, J. P.; Huang, X. H.; Yuan, Y. F.; Chen, X. T.; Mao, F., Preparation and electrochemical performances of cubic shape Cu2O as anode material for lithium ion batteries. *Journal of Alloys and Compounds* **2007,** *441* (1–2), 52-56.

73. Lee, Y. H.; Leu, I. C.; Liao, C. L.; Chang, S. T.; Wu, M. T.; Yen, J. H.; Fung, K. Z., Fabrication and Characterization of Cu2O Nanorod Arrays and Their Electrochemical

Performance in Li-Ion Batteries. *Electrochemical and Solid-State Letters* **2006,** *9* (4), A207-A210.

74. Cabana, J.; Monconduit, L.; Larcher, D.; Palacín, M. R., Beyond Intercalation-Based Li-Ion Batteries: The State of the Art and Challenges of Electrode Materials Reacting Through Conversion Reactions. *Advanced Materials* **2010,** *22* (35), E170-E192.

75. Débart, A.; Dupont, L.; Poizot, P.; Leriche, J.-B.; Tarascon , J. M., A Transmission Electron Microscopy Study of the Reactivity Mechanism of Tailor-Made CuO Particles toward Lithium. *Journal of The Electrochemical Society* **2001,** *148* (11), A1266-A1274.

76. Zhang, W.; Li, M.; Wang, Q.; Chen, G.; Kong, M.; Yang, Z.; Mann, S., Hierarchical Self-assembly of Microscale Cog-like Superstructures for Enhanced Performance in Lithium-Ion Batteries. *Advanced Functional Materials* **2011,** *21* (18), 3516-3523.

77. Park, J. C.; Kim, J.; Kwon, H.; Song, H., Gram-Scale Synthesis of Cu2O Nanocubes and Subsequent Oxidation to CuO Hollow Nanostructures for Lithium-Ion Battery Anode Materials. *Advanced Materials* **2009,** *21* (7), 803-807.

78. Lindsay, M. J.; Skyllas-Kazacos, M.; Luca, V., Anodically synthesized titania films for lithium batteries: Effect of titanium substrate and surface treatment. *Electrochimica Acta* **2009,** *54* (13), 3501-3509.

79. Bao, S.-J.; Bao, Q.-L.; Li, C.-M.; Zhi-Li, D., Novel porous anatase TiO2 nanorods and their high lithium electroactivity. *Electrochemistry Communications* **2007,** *9* (5), 1233-1238.

80. Lindsay, M. J.; Blackford, M. G.; Attard, D. J.; Luca, V.; Skyllas-Kazacos, M.; Griffith, C. S., Anodic titania films as anode materials for lithium ion batteries. *Electrochimica Acta* **2007,** *52* (23), 6401-6411.

81. Barreca, D.; Carraro, G.; Gasparotto, A.; Maccato, C.; Cruz-Yusta, M.; Gómez-Camer, J. L.; Morales, J.; Sada, C.; Sánchez, L., On the Performances of CuxO-TiO2 (x = 1, 2) Nanomaterials As Innovative Anodes for Thin Film Lithium Batteries. *ACS Applied Materials & Interfaces* **2012,** *4* (7), 3610-3619.

82. Lan, C.-K.; Chang, C.-C.; Wu, C.-Y.; Chen, B.-H.; Duh, J.-G., Improvement of the Ar/N2 binary plasma-treated carbon passivation layer deposited on Li4Ti5O12 electrodes for stable high-rate lithium ion batteries. *RSC Advances* **2015,** *5* (112), 92554-92563.

83. Stapleton, P. A.; Goodwill, A. G.; James, M. E.; Brock, R. W.; Frisbee, J. C., Hypercholesterolemia and microvascular dysfunction: interventional strategies. *Journal of Inflammation* **2010,** *7* (1), 1-10.

84. Lloyd-Jones, D.; Adams, R.; Carnethon, M.; De, S. G.; Ferguson, T. B.; Flegal, K.; Ford, E.; Furie, K.; Go, A.; Greenlund, K., Heart disease and stroke statistics--2009 update: a report from the American Heart Association Statistics Committee and Stroke Statistics Subcommittee. *Circulation* **2009,** *119*.

85. Cholesterol Levels: What You Need to Know. *NIH MedlinePlus: the magazine* Summer 2012, pp 6-7.

86. Abell, L. L.; Levy, B. B.; Brodie, B. B.; Kendall, F. E., A Simplified Method for the Estimation of Total Cholesterol in Serum and Demonstration of Its Specificity. *Journal of Biological Chemistry* **1952,** *195* (1), 357-366.

87. Garber, A. M.; Littenberg, B.; Harold C. Sox, J.; Gluck, M. E.; Wagner, J. L.; Duffy, B. M., Costs and Effectiveness of Cholesterol Screening in the Elderly. Office of Technology Assessment: Washington D.C., 1989.

88. Liu, S.; Ju, H., Reagentless glucose biosensor based on direct electron transfer of glucose oxidase immobilized on colloidal gold modified carbon paste electrode. *Biosensors and Bioelectronics* **2003,** *19* (3), 177-183.

89. Ashby, J. N.; Ramasamy, R. P., Molecularly Tethered Cholesterol Oxidase on Multiwall Carbon Nanotubes for Indirect Detection of Cholesterol. *ECS Transactions* **2015,** *69* (41), 1-9.

90. Liang, H.; Jiang, S.; Yuan, Q.; Li, G.; Wang, F.; Zhang, Z.; Liu, J., Co-immobilization of multiple enzymes by metal coordinated nucleotide hydrogel nanofibers: improved stability and an enzyme cascade for glucose detection. *Nanoscale* **2016,** *8* (11), 6071-6078.

91. Rusling, J. F., Enzyme Bioelectrochemistry in Cast Biomembrane-Like Films. *Accounts of Chemical Research* **1998,** *31* (6), 363-369.

92. Abad, J. M.; Gass, M.; Bleloch, A.; Schiffrin, D. J., Direct Electron Transfer to a Metalloenzyme Redox Center Coordinated to a Monolayer-Protected Cluster. *Journal of the American Chemical Society* **2009,** *131* (29), 10229-10236.

93. Cracknell, J. A.; Vincent, K. A.; Armstrong, F. A., Enzymes as Working or Inspirational Electrocatalysts for Fuel Cells and Electrolysis. *Chemical Reviews* **2008,** *108* (7), 2439-2461.

94. Léger, C.; Bertrand, P., Direct Electrochemistry of Redox Enzymes as a Tool for Mechanistic Studies. *Chemical Reviews* **2008,** *108* (7), 2379-2438.

95. Rafighi, P.; Tavahodi, M.; Haghighi, B., Fabrication of a third-generation glucose biosensor using graphene-polyethyleneimine-gold nanoparticles hybrid. *Sensors and Actuators B: Chemical* **2016,** *232*, 454-461.

96. Ramasamy, R. P.; Luckarift, H. R.; Ivnitski, D. M.; Atanassov, P. B.; Johnson, G. R., High electrocatalytic activity of tethered multicopper oxidase-carbon nanotube conjugates. *Chemical Communications* **2010,** *46* (33), 6045-6047.

97. Zhou, Y.; Umasankar, Y.; Ramasamy, R. P., Laccase-TiO2 Nanoconjugates as Catalysts for Oxygen Reduction Reaction in Biocathodes. *Journal of The Electrochemical Society* **2015,** *162* (14), H911-H917.

98. Umasankar, Y.; Ramasamy, R. P., Enhanced Electron Transfer in Enzymatic Bioelectrodes by a Poly(vinyl alcohol) N-Methyl-4(4′-formylstyryl) Pyridinium Methosulfate Acetal Cationic Polymer. *ChemElectroChem* **2014,** *1* (11), 1834-1839.

99. Berg, J.; Tymoczko, J.; Stryer, L., *Biochemistry*. 5th ed.; W H Freeman: New York, 2002.

100. Vasylieva, N.; Maucler, C.; Meiller, A.; Viscogliosi, H.; Lieutaud, T.; Barbier, D.; Marinesco, S., Immobilization Method to Preserve Enzyme Specificity in Biosensors: Consequences for Brain Glutamate Detection. *Analytical Chemistry* **2013,** *85* (4), 2507-2515.

101. Clark, L. C.; Lyons, C., ELECTRODE SYSTEMS FOR CONTINUOUS MONITORING IN CARDIOVASCULAR SURGERY. *Annals of the New York Academy of Sciences* **1962,** *102* (1), 29-45.

102. Sekretaryova, A. N.; Beni, V.; Eriksson, M.; Karyakin, A. A.; Turner, A. P. F.; Vagin, M. Y., Cholesterol Self-Powered Biosensor. *Analytical Chemistry* **2014,** *86* (19), 9540-9547.

103. Abdelwahab, A. A.; Won, M.-S.; Shim, Y.-B., Direct Electrochemistry of Cholesterol Oxidase Immobilized on a Conducting Polymer: Application for a Cholesterol Biosensor. *Electroanalysis* **2010,** *22* (1), 21-25.

104. Li, Z.; Xie, C.; Wang, J.; Meng, A.; Zhang, F., Direct electrochemistry of cholesterol oxidase immobilized on chitosan–graphene and cholesterol sensing. *Sensors and Actuators B: Chemical* **2015,** *208*, 505-511.

105. Cao, S.; Zhang, L.; Chai, Y.; Yuan, R., Electrochemistry of cholesterol biosensor based on a novel Pt–Pd bimetallic nanoparticle decorated graphene catalyst. *Talanta* **2013,** *109*, 167-172.

106. Matharu, Z.; Arya, S. K.; Singh, S. P.; Gupta, V.; Malhotra, B. D., Langmuir–Blodgett film based on MEH-PPV for cholesterol biosensor. *Analytica Chimica Acta* **2009,** *634* (2), 243-249.

107. Dhyani, H.; Azahar Ali, M.; Pandey, M. K.; Malhotra, B. D.; Sen, P., Electrophoretically deposited CdS quantum dots based electrode for biosensor application. *Journal of Materials Chemistry* **2012,** *22* (11), 4970-4976.

108. Rahman, M. M.; Li, X.-b.; Kim, J.; Lim, B. O.; Ahammad, A. J. S.; Lee, J.-J., A cholesterol biosensor based on a bi-enzyme immobilized on conducting poly(thionine) film. *Sensors and Actuators B: Chemical* **2014,** *202*, 536-542.

109. Li, X.-R.; Xu, J.-J.; Chen, H.-Y., Potassium-doped carbon nanotubes toward the direct electrochemistry of cholesterol oxidase and its application in highly sensitive cholesterol biosensor. *Electrochimica Acta* **2011,** *56* (25), 9378-9385.

110. Smith, E. W.; Skelton, M. S.; Kremer, D. E.; Pascoe, D. D.; Gladden, L. B., Lactate distribution in the blood during progressive exercise. *Medicine and Science in Sports and Exercise* **1997,** *29* (5), 654-660.

111. Aronoff, S. L.; Berkowitz, K.; Shreiner, B.; Want, L., Glucose Metabolism and Regulation: Beyond Insulin and Glucagon. *Diabetes Spectrum* **2004,** *17* (3), 183-190.

112. Jones, C. M.; Mack, K. A.; Paulozzi, L. J., PHarmaceutical overdose deaths, united states, 2010. *JAMA* **2013,** *309* (7), 657-659.

113. Edwards, N. L.; Goldman, L.; Schafer, A. I., Crystal Deposition Diseases. In *Goldman-Cecil Medicine*, 25 ed.; Elsevier/Saunders: Philadelphia, PA, 2016; Vol. 2, pp 1811-1816.